Testing and analysis of additively manufactured stainless steel corrugated cylindrical shells in compression

Ruizhi Zhang [1], Leroy Gardner [2], Mohsen Amraei [3], Craig Buchanan [4], Heidi Piili [5]

[1] Research Associate, Department of Civil and Environmental Engineering, Imperial College London, London SW7 2AZ, UK (corresponding author). Email: r.zhang18@imperial.ac.uk

[2] Professor, Department of Civil and Environmental Engineering, Imperial College London, London SW7 2AZ, UK. Email: leroy.gardner@imperial.ac.uk

[3] Lecturer, Department of Mechanical Engineering, University of Turku, Turku 20520, Finland. Email: mohsen.amraei@utu.fi

[4] Lecturer, Department of Civil and Environmental Engineering, Imperial College London, London SW7 2AZ, UK. Email: craig.buchanan@imperial.ac.uk

[5] Senior Research Fellow, Department of Mechanical Engineering, University of Turku, Turku 20520, Finland. Email: heidi.piili@utu.fi

Abstract

Initial geometric imperfections have been identified as the main cause for the large discrepancies between experimental and theoretical buckling loads of thin-walled circular cylindrical shells under axial compression. The extreme sensitivity to imperfections has been previously addressed and mitigated through the introduction of stiffeners; however, sensitivity still remains. Optimized corrugated cylindrical shells are largely insensitive to imperfections and hence exhibit excellent load-bearing capacities, but their complex geometries make their construction difficult and costly using conventional manufacturing techniques. This was overcome in the present study through additive manufacturing (AM). Nine optimized corrugated shells with different diameter-to-thickness ratios, together with one reference circular cylindrical shell, were additively manufactured by means of powder bed fusion (PBF) from austenitic and martensitic precipitation hardening stainless steel. The structural behavior of the AM shells was then investigated experimentally, with the testing program comprising tensile coupon tests, measurements of basic geometric properties and axial compression tests. Numerical analyses were also conducted following completion of the physical experiments. The experimental and numerical results verified the effectiveness of optimized corrugated cylindrical shells in achieving improved local buckling capacity and reduced imperfection sensitivity. Initial recommendations for the structural design of the studied cross-sections are made.

Keywords: Additive manufacturing; Compressive testing; Corrugated cylindrical shells; Current design approaches; EN 1993-1-6; Finite element modeling; Imperfection sensitivity; Optimization; Stainless steel; 3D printing.

1. Introduction

Cylindrical shells are one of the most commonly-used type of structural component in the aerospace, offshore, civil and other engineering industries due to their excellent combination of light weight and high strength (Niloufari et al. 2014). Numerous experimental investigations into the buckling behavior of axially compressed cylindrical shells have been carried out (Hilburger et al. 2006; NASA 1968; Wagner et al. 2017; Weingarten et al. 1965), and a large disparity between theoretical and experimental buckling loads has been observed due to the presence of initial imperfections (NASA 1968; Teng et al. 2005). To allow for the effects of imperfections in engineering practice, empirical knock-down factors, such as those presented in NASA SP-8007 (2020), are widely used to penalize the theoretical elastic buckling loads, particularly in the preliminary design of cylindrical shell structures. A generic buckling capacity curve is employed in EN 1993-1-6 (CEN 2017), where the buckling strength is determined relative to the plastic load as a function of the relative slenderness of the shell.

The addition of stiffeners, such as stringers and rings, has been shown to be effective in improving the buckling resistance of thin-walled shell structures; stiffeners have thus been used extensively in structural engineering applications. However, imperfection sensitivity still remains (Hutchinson and Frauenthal 1969; Singer et al. 1971), and the manufacture of stiffeners is often impractical and costly. Intrinsically stiffened shells, such as pseudo-cylindrical concave polyhedral shells (Knapp 1977; Yoshimura 1955), 'Aster' shells (Araar et al. 1998; Combescure and Jullien 2015) and free-form wavy cylindrical shells (Ning and Pellegrino 2015, 2017), have also been developed, with the latter two types having corrugated rather than circular cross-sections and achieving higher strength from their waviness. The potential of corrugated cylindrical shells, in terms of reduced imperfection sensitivity and enhanced load-bearing capacities, can be readily exploited through additive manufacturing. Additive manufacturing (AM), also referred to as 3D printing, has been receiving growing attention in recent years owing (Kanyilmaz et al. 2022; Huang et al. 2022; Gardner Submitted), in part, to its ability to produce complex structures, particularly those generated through optimization (Ye et al. 2021). In the present study, the structural performance, load-bearing resistance and imperfection sensitivity of nine optimized, additively manufactured corrugated cylindrical shells with different diameter-to-thickness ratios, together with one reference circular cylindrical shell, are examined experimentally. The test specimens were produced from stainless steel by powder bed fusion (PBF). Material coupon tests, initial geometric measurements and compression tests are described; the results are used to demonstrate the benefits that could be derived from the optimized corrugated geometries. A parallel numerical study involved the validation of finite element models and the subsequent generation of additional resistance data through parametric studies. Finally, the applicability of existing design methods to the studied corrugated cross-sections produced by PBF, is evaluated.

2. Experimental investigation

An experimental program to investigate the cross-sectional behavior of optimized corrugated cylindrical shells produced by PBF, comprising tensile coupon tests, initial geometric measurements and axial compression tests, is described in this section. Two different stainless steel grades were adopted – austenitic grade 316L (also referred to as EN 1.4404 and X2CrNiMo17-12-2), which is widely used in the aerospace, marine, chemical and construction industries due to its excellent combination of high mechanical strength, corrosion resistance and good weldability characteristics (Kianersi et al. 2014), and a commercial martensitic precipitation hardening (PH) grade CX (with similar chemical composition to PH 13-8 Mo), which has many potential applications in the aerospace, marine, defense, nuclear and injection molding industries due to its excellent strength, corrosion resistance, hardness and toughness (Asgari and Mohammadi 2018; Sanjari et al. 2020). Two Aster shells and five free-form wavy shells with various diameter-to-thickness ratios, were manufactured by PBF using the 316L stainless steel powder. One Aster shell and one wavy shell, along with a reference circular cylindrical shell with a nominal outer diameter D of 200 mm and thickness of 1.0 mm, were produced by PBF using the CX stainless steel powder. The nominal chemical composition and material properties of PBF parts produced using the EOS 316L and CX stainless steel powders, as provided in the manufacturer's data sheet (EOS 2017, 2019), are shown in Tables 1 and 2, respectively. The coupons and shell specimens were manufactured in the Laboratory of Laser Processing of the School of Energy Systems at LUT University, while the tensile coupon tests and compression tests were performed in the Structures Laboratory of the Department of Civil and Environmental Engineering at Imperial College London.

The corrugated cross-section profiles were established following the approach developed by Reitinger et al. (1994, 1995), with geometrically and materially nonlinear analysis incorporated into the optimization process. Typical (one quarter) examples of Aster and wavy cross-section profiles are shown in Fig. 1, where r is the radius of the reference circular shell, Δr is the maximum allowable radial deviation, ρ_{max} and ρ_{min} are the upper and lower radius limits for the control points, and ρ_i and θ_i are the radial and circumferential positions of the trace points (or control points) lying on the curves. Details of the employed optimization method and a direct assessment of mass efficiency have been reported by Zhang et al. (2021b, 2022), but since the manufacture and compression testing of the corrugated shells utilize the optimization results, a brief summary of their design is presented herein. The objective function was the ultimate stress f_{ult} of the corrugated cylindrical shells, as given by:

$$f_{ult} = \frac{\min(P_0, P_+, P_-)}{A} \quad (1)$$

where P_0, P_+ and P_- are the buckling loads of the perfect shell and imperfect shells with positive and negative imperfections, respectively, and A is the cross-sectional area. The wave numbers and amplitudes of the Aster cross-section, along with the radial positions of the control points lying on a quarter of the wavy cross-section, were considered to be the optimization variables. The nominal cross-section sizes (outer diameter D × thickness t) of the circular (C200×1.0), Aster (A200×1.0, A180×0.7 and A200×0.7) and wavy (W150×1.0, W180×1.0, W200×1.0, W150×0.7, W180×0.7 and W200×0.7) cylindrical shells, together with the associated optimization parameters, are listed in Table 3, where L is the nominal length, ω_a is the assumed imperfection amplitude, corresponding to Class B fabrication quality in EN 1993-1-6 (CEN 2017) for the 316L stainless steel shells and to the thickness t for the CX stainless steel shells, Δr is the maximum allowable radial deviation from the reference circle, M is the number of half waves of the Aster cross-section and N is the number of control points lying on one quarter of the wavy cross-section profile, which is 4-fold rotationally or mirror symmetric to the profiles in other quadrants. The cross-section profiles of the final printed Aster and wavy shells are shown in Figs. 2 and 3, where the control points lying on the wavy cross-section profile are highlighted, and the radial positions of the control points are provided in Table 4. The optimization results of the examined Aster and wavy shells, together with the results of their reference circular cylindrical shells, are summarized in Table 5, where l_p is the centerline perimeter, σ_{cr} is the elastic local buckling stress, γ is the imperfection sensitivity factor that describes the sensitivity of the buckling resistance to the local imperfection amplitude, defined by Eq. (2), and $f_{ult,cyl}$ is the ultimate stress of the reference circular cylindrical shell.

$$\gamma = \frac{\min(P_+, P_-)}{P_0} \tag{2}$$

2.1 Manufacture of specimens

All coupons and shell specimens were built using a modified PBF EOS M 290 research machine with a maximum construction size of approximately 250 mm×250 mm×325 mm. The PBF manufacturing process involves the layering of metallic powder that is fused by a high-energy laser beam to build the final components; a more detailed description of this process is provided in Zhang et al. (2021a). The processing parameters set by the machine manufacturers are presented in Table 6 (EOS 2017, 2019). The 316L and CX stainless steel shells and the 316L stainless steel coupons were printed vertically, with their longitudinal axis perpendicular to the print layers (i.e. θ=90°, where θ is the angle between the longitudinal axis of the coupon and the build plate); the CX stainless steel coupons were, unintentionally, built horizontally (i.e. θ=0°) rather than vertically, as shown schematically in Fig. 4. However, PBF CX stainless steel has been found to have a weak crystallographic texture and hence low anisotropy (Afkhami et al. 2022). The stress-strain curves obtained from the horizontal coupons can therefore also be expected to be representative of the response in the vertical direction; this argument is further supported by the ability of the FE models presented in Section 3, to which the measured stress-strain curves from the horizontal coupons were assigned, to match the experimental behavior of the shells. Photographs of typical circular, Aster and wavy cylindrical shell specimens are shown in Figs. 5 and 6. Fig. 7 shows photographs of three corrugated shell specimens within the same batch during and after printing.

2.2 Tensile coupon tests

Six dog-bone shaped tensile coupons were printed using both the 316L and CX stainless steel powders, leading to 12 coupons in total; the nominal dimensions of the coupons are shown in Fig. 8. Standard gauge lengths equal to $5.65\sqrt{S_0}$, where S_0 is the original cross-sectional area of the parallel length, were scribed onto both coupon faces for the post-test calculation of fracture strains.

The tensile coupon tests were conducted using an Instron 8802 250 kN hydraulic testing machine, as shown in Fig. 9. Random speckle patterns were sprayed onto the front and back faces of the coupons prior to testing and captured using a four-camera LaVision digital image correlation (DIC) system during the tests. The testing machine was driven under displacement control in accordance with EN ISO 6892-1 (CEN 2016); the crosshead separation rates were determined such that a strain rate of 0.007% s^{-1} up to the 0.2% proof stress and of 0.025% s^{-1} after yielding was attained, with a gradual ramp between them to prevent any abrupt changes in stress. The applied loads and DIC images were recorded at 1-second intervals. The sequence of the DIC images was post-processed to obtain the deformation and strain fields using the initial positions as a reference. The longitudinal strain was determined by averaging the strains over the parallel length of both coupon faces, and the stress was obtained using the measured applied load and cross-sectional area.

The measured engineering stress-strain curves obtained from the 316L and CX stainless steel coupons are plotted in Figs. 10 and 11, respectively, while the key material properties, including the Young's modulus E, 0.2% proof strength $\sigma_{0.2}$, 1.0% proof strength $\sigma_{1.0}$, ultimate tensile strength σ_u and corresponding strain ε_u, fracture strain over the marked gauge length ε_f, Ramberg-Osgood parameter n (Ramberg and Osgood 1943) and the extended strain hardening parameters $m_{1.0}$ and m_u (Gardner and Ashraf 2006; Mirambell and Real 2000; Rasmussen 2003; Yun et al. 2021) that were fitted to the measured stress-strain curves using the methods described in Arrayago et al. (2015) and Gardner and Yun (2018), are reported in Tables 7 and 8. The measured 0.2% proof stress, ultimate stress and fracture strain were comparable to those reported in the EOS material datasheet (EOS 2017, 2019). The Young's moduli of the examined PBF 316L and CX stainless steels were found to be slightly lower than the typically assumed value of E=200000 N/mm^2 for conventional stainless steels (Arrayago et al. 2015). The PBF CX stainless steel exhibited much higher proof and ultimate strengths, but lower fracture strains than those of the PBF 316L stainless steel. The correlation between the mechanical properties of the PBF 316L and CX stainless steels and their microstructural characteristics, is further discussed in Zhang et al. (2022).

2.3 Geometric measurements

Prior to end potting, the geometric properties of the shell test specimens were determined through (i) hand measurements using digital calipers, (ii) Archimedes' method, which is useful for determining the volume of irregular objects, and (iii) laser scanning – an advanced 3D full-field measurement technique. The setups for the latter two measuring techniques are shown in Fig. 12. The length L and wall thicknesses t (at both ends) at the peak, trough and middle points of each corrugation of the specimens were measured using calipers. The weights of each specimen in air W_{air} and in water W_{water} were measured using a high-precision balance, and the volume V_{Arch} and the density ρ were calculated based on Archimedes' method (see Eqs. (3) and (4)). An average density of 7.55×10^3 kg/m^3 and 7.54×10^3 kg/m^3 was obtained for the 316L and CX stainless steels based on the weight and volume measurement data, respectively.

$$V = \frac{W_{\mathrm{air}} - W_{\mathrm{water}}}{\rho_{\mathrm{w}} g} \tag{3}$$

$$\rho = \frac{W_{\mathrm{air}}}{gV} \tag{4}$$

The volume V_{Laser}, cross-sectional area A_{Laser} and geometric imperfection distribution can also be determined through laser scanning. The external and internal surface geometries of the shell specimens were measured using a Faro ScanARM laser scanner and pre-processed in Geomagic Wrap (version 2017.0.2:64); the workflow for processing the raw scanned geometric data from laser scanning is shown in Fig. 13. The pre-processed 3D point data were converted into a polygon model and imported into Rhino 3D (version 5 SR14 64-bit); the model was then aligned with the global coordinate system and sectioned into cross-section slices along the specimen length. The average cross-sectional area A_{Laser} for each specimen was then determined, and compared with that obtained through Archimedes' method (i.e. the volume V_{Arch} divided by the specimen length L_{cal}), as shown in Table 9. Note that the cross-sectional areas obtained from laser scanning were all within 2% of those obtained using Archimedes measurements, but were considered to be less reliable due to the difficulty in accurately detecting the corner and edge features, i.e. the peaks and troughs of the shell corrugations (Zhang et al. 2021c); thus, the measured cross-sectional areas obtained from Archimedes' method A_{Arch} rather than those from laser scanning A_{Laser} are utilized for the analysis of the experimental results presented hereinafter.

Measurements of local imperfections were carried out based on the geometry captured using 3D laser-scanning. First, a series of vertical planes were established through the cross-section slices to create sets of longitudinal points along the specimen length. A straight line was fitted to each set of longitudinal points using linear regression to serve as a reference datum from which the deviations were defined, representing the local imperfections (Meng and Gardner 2020a; Zhang et al. 2021a); a schematic for the determination of the longitudinal imperfections using laser scan data is shown in Fig. 14. Typical measured imperfection distributions for the circular, Aster and wavy cylindrical shells (specimens C200×1.0, A200×1.0 and W200×0.7) are shown in Figs. 15-17, where outward and inward deviations are denoted as positive and negative, respectively. The maximum absolute deviation over the entire specimen was taken as the local imperfection amplitude ω_{max}, which lay between 0.14 mm and 0.73 mm (corresponding to 0.2t~t), as reported in Table 9. An analysis of imperfection amplitude data associated with the slenderness or thickness of the shell specimens revealed no clear trend.

A probabilistic analysis was also conducted to assess the variation in longitudinal imperfection amplitudes around the perimeter of the shell specimens. Histograms of 360 local imperfection amplitude measurements (at intervals of 1°) were constructed, and are presented for a typical circular, Aster and wavy cylindrical shell in Figs. 15-17, respectively, as well as the empirical cumulative distribution function (CDF) curves for the 360 measurements. A CDF value describes the probability that a randomly selected imperfection amplitude $\mathbf{\Delta}$ will be less than a given imperfection amplitude value ω_p, i.e. $P(\mathbf{\Delta} < \omega_p)$ (Schafer et al. 1996; Schafer and Peköz 1998). Imperfection values for various probabilities along with the mean and standard deviation for each specimen are summarized in Table 10. Suitable imperfection amplitudes based on the CDF values can be utilized in finite element (FE) modeling, as recommended by Yu and Schafer (2005). The $P(\mathbf{\Delta}<\omega_p)$=95% imperfection value $\omega_{95\%}$ represents an imperfection amplitude that would not be expected to be exceeded in 95% of PBF shell specimens; use of this imperfection amplitude is assessed in the FE model validation presented in Section 3.2. All dimensions and CDF values with corresponding imperfection amplitudes for the shell test specimens are summarized in Table 9.

2.4 Compression tests

A total of ten axial compression tests were performed to ascertain the compressive behavior and load-bearing capacity of the circular, Aster and free-form wavy cylindrical shells manufactured by PBF. For each shell specimen, the printed (top) end exhibited a high level of production accuracy, while the lower end that was detached from the build plate had to be machined flat and square, removing any remaining support structures, to ensure uniform load introduction during testing. Wooden blocks were precisely machined and inserted into the specimens to reinforce the clamped regions during end machining, as shown in Fig. 18(a). The circular cylindrical shell C200×1.0 was found to have an unexpected crack near its end; the end segment containing the crack was removed and discarded, resulting in a final length of 152.7 mm, shorter than the original intended length of 200.0 mm. Prior to testing, the top and bottom ends of each specimen were restrained using Araldite 2011 epoxy adhesive potting, supported by external and internal metallic ring stiffeners with a thickness of 10 mm, in order to prevent premature end failure, as shown in Fig. 18(b).

All the compression tests were performed using an Instron 3500 kN hydraulic testing machine; the test setup is shown in Fig. 19. A ball seating was mounted onto the crosshead of the testing machine to accommodate any possible gaps between the specimens and the end platens and to ensure that uniform axial loading was applied to the cylinder edges. Hardened end platens were positioned at both ends of the specimens to avoid damage to the testing machine from the high levels of localized stresses. Prior to testing, the surface of each specimen was spray-painted with a matte white background and a random black speckle pattern of sizes larger than 3 to 5 pixels to create trackable features for DIC. A four-camera LaVision DIC system was employed to monitor the relative movement of the speckles from two sides at 90° to each other, with two cameras detecting each side; the DIC system layout is schematically shown in Fig. 20. The axial deformations were recorded using three potentiometers positioned at 120° intervals and three equally spaced strain gauges attached to each specimen at mid-height, as shown in Fig. 19. The compressive load was introduced through displacement control to achieve a compressive strain rate of approximately 0.1% min^{-1}, and captured using a load cell within the testing machine. The key test outputs – the axial load, top platen movement, potentiometer and strain gauge readings and DIC images, were recorded at a frequency of 1 Hz. Post-test correlation and analysis were conducted on the captured DIC images using Davis 8 (version 8.4.0) with a subset size of 19×19 pixels (to contain 4 to 10 speckles in each subset), a 5-pixel step size and a strain smoothing filter to obtain the surface deformation and strain fields of the specimens.

The post-ultimate distributions of out-of-plane deformations of all test specimens are presented in Figs. 21-23 for better visualization of the failure modes, where positive (colored in red) and negative (colored in purple) deformations are outward and inward, respectively. Note that the speckle images and processed displacements could have relatively large rotations or distortions in the non-overlapped regions, especially in the troughs and the two sides of the measured lateral surfaces, while the axial displacements derived from the central lateral face were found to have small stereo reconstruction errors and were thus adopted for the experimental data analysis, including the construction of the load-end shortening curves. The circular cylindrical shell (C200×1.0) buckled locally in an asymmetric 'chequerboard' pattern with one half longitudinal wave and 7 circumferential waves. The Aster shells deformed in an axisymmetric mode with outward bulging; no visible local buckles were observed near the peak load, but after testing, there were localized buckles in the troughs of the corrugations, as shown in Fig. 22. The free-form wavy shells also deformed an axisymmetric mode and failed by local buckling in the troughs of the corrugations and in the regions of minimum curvature (see Fig. 23).

Typical axial load-end shortening curves and DIC results from the compression tests on the circular (C200×1.0), Aster (A200×1.0) and wavy (W200×1.0) cylindrical shells, are presented in Figs. 24-26, where the evolution of the axial strain fields can be clearly observed. All axial load-end shortening curves obtained from (i) the potentiometer and strain gauge readings, with the elastic deformations of the end platens eliminated (Centre for Advanced Structural Engineering 1990; Yun et al. 2018), and (ii) the DIC data, are plotted in Fig. 27. The two approaches to the calculation of end shortenings were shown to yield essentially identical results. The buckling of the circular cylindrical shell occurred abruptly, with an audible 'snap' and a sudden drop in the applied load; the shell stablished again at about half of the peak load. The Aster and free-form wavy shells, on the other hand, exhibited a more gentle failure. The key test results – the peak load N_u, the end shortening at the peak load δ_u, the ratio of the peak load N_u to the plastic load $\sigma_{0.2}A$ (i.e. equivalent, in terms of stresses, to $f_{ult}/\sigma_{0.2}$), and the ratio of the normalized ultimate load of the Aster or wavy shells to that of the reference circular cylindrical shells expressed, in terms of stresses, as $f_{ult}/f_{ult,cyl}$, are summarized in Table 9. All wavy shells, except the specimen W200×0.7, and the Aster shell with the largest wave amplitude failed at a load level around or beyond the plastic load $\sigma_{0.2}A$, while failure of the other Aster shells and all circular shells occurred below this load level. The different levels of increase in load-carrying capacity of the specimen W200×1.0 relative to the specimen W180×1.0 are attributed mainly to the different material grades, which affect slenderness, and printing accuracy. Regarding the shell specimens built from CX stainless steel, the Aster and wavy shells showed a 33% and 46% increase in failure stress respectively when compared to the circular cylindrical shell. This increase in failure stress is lower than the expected 180% value; this is attributed to the better-than-expected performance of the circular shell due to the lower measured imperfection amplitude than the value assumed in the initial predictions (Zhang et al. 2021b).

3. Numerical simulations

In parallel with the experimental program, a numerical simulation study of the compressive cross-sectional behavior of corrugated cylindrical shells produced by PBF was undertaken. FE models based on the measured geometries and material properties were first developed and validated against the experimental results. Parametric studies were then conducted using the validated models to generate additional buckling reduction factors for corrugated cylindrical shells.

3.1 Description of FE models

Geometrically and materially nonlinear analyses without and with imperfections (GMNA, GMNIA) were carried out using the software package Abaqus version 2017 to simulate the cross-sectional behavior of corrugated cylindrical shells under axial compression. The four-noded shell element with reduced integration, S4R, was adopted as the element type. A mesh size of $0.2(Dt)^{1/2}$, which was found to be sufficiently fine for capturing the local buckling behavior of circular hollow sections with good computational efficiency (Meng et al. 2020; Meng and Gardner 2020b; Zhang et al. 2021a), was found to be also suitable for wavy and Aster shells and was thus utilized in this study. The fixed-ended boundary conditions employed in the tests were simulated by coupling the end sections of the shells to reference points, where only longitudinal displacement of the top reference point was allowed, as shown in Fig. 28. The adopted material stress-strain curves for the 316L and CX stainless steels (see Figs. 10 and 11) were constructed from the two-stage Ramberg-Osgood parameters (E, $\sigma_{0.2}$, n, σ_u, ε_u, and m_u) averaged from the measured properties, as reported in Tables 7 and 8. The resulting stress-strain relationships were converted into true stress and plastic strain and inputted into the FE analyses. For the parametric studies, only the material stress-strain curve for PBF 316L stainless steel in the vertical (θ=90°) direction was employed.

Initial geometric imperfections were considered in two ways. In Method 1, imperfect shell models were reconstructed directly from the scan data points, while in Method 2, eigenmode-affine imperfection patterns, scaled by a measured imperfection value, were employed. For Method 1, the scan data were pre-processed in Geomagic Wrap and imported in Rhino in the form of a polygon model, which was contoured into transverse slices at a spacing of 1 mm and then radially sectioned into points at intervals of 1°. The data points were regenerated into an interpolated curve and then a smooth surface was fitted; the generated Initial Graphics Exchange Specification (IGES) files were imported into Abaqus as shell models and used in the GMNIA. For Method 2, the lowest eigenmode from a prior linear bifurcation analysis (LBA) was used to represent the local geometric imperfection pattern and was factored by measured imperfection amplitudes in the GMNIA.

3.2 Validation

The accuracy of the established FE shell models was evaluated by comparing the FE results with the key test outputs in terms of the ultimate loads, load-deformation histories and failure modes. Comparative studies were undertaken considering both measured geometries and eigenmode-affine geometric imperfection shapes with different amplitudes. Four groups of FE analyses were carried out: (i) GMNA on the perfect shells, (ii) GMNIA on the scanned shell geometries, (iii) GMNIA on the shells with the LBA mode shape scaled by the measured $\omega_{95\%}$ and (iv) GMNIA on the shells with the LBA mode shape scaled by the measured ω_{max}.

The ratios of the numerical to experimental ultimate loads $N_{u,FE}/N_{u,test}$ and corresponding deformations $\delta_{u,FE}/\delta_{u,test}$ for the four different local imperfection patterns and amplitudes, are reported in Table 11, where COV is the coefficient of variation. It can be seen from the comparisons that the use of the scanned geometries yields the most accurate on average and least scattered predictions of the ultimate loads and corresponding deformations. The numerical load-deformation curves from the FE models with the scanned geometries are plotted in Fig. 29; the developed FE models were found to accurately replicate the observed test responses. Note that the shell specimens made from the CX stainless steel were printed vertically (i.e. θ=90°), while the available material data were derived from the tensile tests on horizontally printed coupons (i.e. θ=0°); use of the material properties from the horizontal coupon tests in the FE models yielded good agreement with the test results, indicating low anisotropy in the studied CX stainless steel. The local imperfection modeling technique that employed the lowest eigenmode pattern and measured amplitude ω_{max} was also found to accurately predict the buckling response of the examined shells, as shown in the comparisons of the load-deformation histories (see Fig. 30) and typical failure modes obtained using the lowest eigenmode pattern and measured amplitude ω_{max} (see Fig. 31).

As can be seen from Table 11, the load-carrying capacities of the Aster and wavy shell specimens were almost insensitive to imperfections, while the circular cylindrical shell C200×1.0 with the measured imperfection amplitude ω_{max} of only 0.19 mm exhibited an approximately 20% reduction in load-bearing capacity relative to the perfect shell. This dramatic difference in imperfection sensitivity can also explain the numerical ultimate loads and corresponding deformations obtained using ω_{max} and $\omega_{95\%}$ being quite close for all corrugated shells, but not for the reference circular shell. Overall, it can be concluded that FE simulations featuring either direct modeling of imperfections (i.e. through the use of scan data) or using eigenmode shapes with measured imperfection amplitudes can accurately replicate the buckling behavior of thin-walled circular and corrugated cylindrical shells manufactured by PBF; the developed models are therefore considered to be suitable for use in parametric studies.

3.3 Parametric studies

Upon validation of the developed FE models, parametric studies were conducted to generate numerical data to cover a wider range of cross-sectional slendernesses, numbers of waves and amplitudes of corrugations, with a focus on the Aster shells. The free-form wavy shells cannot be easily parameterized with only a few geometric variables, and were thus not included in the parametric studies despite their slightly better performance than the Aster shells. Class B imperfection amplitudes, determined according to EN 1993-1-6 (CEN 2017), were assumed. Four shell slendernesses were considered for the reference circular shells, with diameter D × thickness t of A150×1.0, A180×1.0, A180×0.7 and A200×0.7. The number of half waves was varied between 4 and 30, while the wave amplitude was varied from 1 mm to 25 mm. The length of the modeled shells was set equal to the outer diameter of the reference circular cross-sections. In total, 2764 cross-sectional axial compression resistance results were generated in the numerical simulations. The numerical results are presented, and used together with the experimental data for the assessment of existing design methods in the following section.

4. Comparisons with existing design provisions

4.1 Introduction

The applicability of existing structural design rules to the studied additively manufactured corrugated profiles is appraised in this section. Emphasis is placed on the European design code for steel shell structures, EN 1993-1-6 (CEN 2017), but comparisons are also made with the provisions of EN 1993-1-4 (CEN 2015) and EN 1993-1-5 (CEN 2006) for stainless steel and plated structures, respectively. The accuracy of the design rules is assessed through comparisons of the experimental and numerical ultimate loads with the predicted ultimate loads. In the comparisons, the measured (or modeled) material properties and geometries are used in the resistance calculations, and all partial factors for resistance are set to unity. A total of 10 experimental and 2764 numerical data points pertaining to axially compressed stainless steel corrugated cylindrical shells manufactured by PBF are considered.

4.2 Design provisions

For the design of stainless steel CHS with local slenderness values $D/t\varepsilon^2$ up to 250, EN 1993-1-4 (CEN 2015) employs the concept of effective area A_{eff}, which can be expressed in terms of the buckling reduction factor χ through Eq. (5).

$$\chi = \frac{A_{eff}}{A} \tag{5}$$

For more slender shells, reference is made to EN 1993-1-6 (CEN 2017), which employs a generic three-stage capacity curve (see Fig. 32) that relates the dimensionless buckling resistance χ (equal to R_k/R_{pl}) of a shell to its relative slenderness $\bar{\lambda}_c$ defined by Eq. (6), where R_k is the characteristic buckling load factor, and R_{pl} and R_{cr} are the load factors at the plastic limit and elastic critical buckling condition, respectively.

$$\bar{\lambda}_c = \sqrt{R_{pl} / R_{cr}} \tag{6}$$

The relative buckling strength χ, involving the hardening limit χ_h, the squash limit slenderness $\bar{\lambda}_0$, the elastic buckling reduction factor α, the plastic range factor β, the interaction exponent factor η and the plastic limit relative slenderness $\bar{\lambda}_p$, can be calculated from Eq. (7).

$$\chi = \begin{cases} \chi_h - \bar{\lambda}_c / \bar{\lambda}_0 \left(\chi_h - 1\right) & \text{when } \bar{\lambda}_c \leq \bar{\lambda}_0 \\ 1 - \beta \left(\dfrac{\bar{\lambda}_c - \bar{\lambda}_0}{\bar{\lambda}_p - \bar{\lambda}_0} \right)^{\eta} & \text{when } \bar{\lambda}_0 < \bar{\lambda}_c < \bar{\lambda}_p \\ \dfrac{\alpha}{\bar{\lambda}_c^{\,2}} & \text{when } \bar{\lambda}_p \leq \bar{\lambda}_c \end{cases} \tag{7}$$

The capacity parameters for medium-length cylinders under uniform axial compression, as specified in EN 1993-1-6 (CEN 2017), are summarised in Table 12, where $\Delta\omega_k = \frac{1}{Q}\sqrt{rt}$ is the characteristic imperfection amplitude, and Q is the fabrication quality parameter. The two reference resistances R_{pl} and R_{cr} would typically be determined by numerical analyses, i.e. materially nonlinear and linear bifurcation analyses (MNA and LBA) respectively. The GMNIA and the experimental results were used to evaluate the EN 1993-1-6 design curve defined by the capacity parameters listed in Table 12.

For steels with nonlinear stress-strain behavior, an elastic-plastic representation that employs a reduced value of the elastic modulus E_{red}, which can be conservatively taken as the secant modulus at the 0.2% proof stress E_{sec}, and the 0.2% proof stress $\sigma_{0.2}$, in place of the Young's modulus E and yield strength f_y, respectively (see Fig. 33), is recommended in EN 1993-1-6 (CEN 2017). Direct comparisons are made between the strength reduction factors obtained from GMNIA (i.e. R_{GMNIA}/R_{pl}) for axially compressed circular cylindrical shells made from 316L stainless steel with various D/t ratios from 20 to 2726 and the design curves using the initial tangent (i.e. Young's) modulus E_0 and the secant modulus at the 0.2% proof stress E_{sec} in Fig. 34, where Class B levels of imperfection amplitudes have been assumed. Note that for the same relative slenderness $\bar{\lambda}_c$, the diameter-to-thickness ratio *D*/*t* is smaller when the secant modulus E_{sec} (rather than the Young's modulus) is employed, leading to different meridional buckling parameters (α, β, η and $\bar{\lambda}_p$) and hence a different buckling curve. It can be seen that use of E_{sec} leads to rather conservative buckling resistance predictions for stainless steel circular cylindrical shells, while the straightforward use of the E_0 is unsafe for stainless steel circular cylindrical shells of medium slenderness. It has been shown in the experiments and numerical simulations that the optimized corrugated shells exhibit behavior more similar to plates than shells, with a stable post-buckling response and reduced imperfection sensitivity. This behavior is attributed to stiffening effect and concentrated zones of compressive stresses in the corrugated cylindrical shell located near the points of minimum radius of curvature, akin to the edges of simply-supported plates. Comparisons are also made in the following sub-section against the strength curve for stainless steel internal plate elements in compression provided in EN 1993-1-4 (CEN 2015; Gardner and Theofanous 2008) and given by:

$$\rho = \frac{0.772}{\bar{\lambda}_c} - \frac{0.079}{\bar{\lambda}_c^{\,2}} \leq 1 \tag{8}$$

and the elastic buckling curve, given by:

$$\chi = \frac{1}{\bar{\lambda}_c^{\,2}} \leq 1 \tag{9}$$

4.3 Assessment of resistance predictions

In this subsection, consideration is given to the design of the studied shells. The numerical results generated from the parametric studies on Aster shells and their reference circular cylindrical shells, together with the experimental data on circular, Aster and wavy shells produced by PBF, are compared with the resistance predictions obtained from existing design provisions, principally those set out in EN 1993-1-6 (CEN 2017). The experimental ultimate loads for the Aster shells (shown by solid squares) and wavy shells (shown by solid triangles) and numerical ultimate loads for the Aster shells (shown by hollow squares) and their reference circular shells (shown by hollow circles), normalized by the corresponding plastic loads, are plotted against their cross-sectional slendernesses in Fig. 35. For the shells in the very low relative slenderness range, values of relative buckling strength χ greater than unity arise due to the effect of material strain hardening (Ashraf et al. 2006; Yuan et al. 2014). In Fig. 35(a), the initial tangent modulus E_0 is employed, while in Fig. 35(b), the secant modulus at 0.2% proof stress E_{sec} is used. The plastic loads of the stainless steel shells were taken equal to $\sigma_{0.2}A$, while the elastic critical loads were determined using LBA. The EN 1993-1-6 strength curves, alongside the elastic buckling and EN 1993-1-4 (CEN 2015) plate buckling curves, are also presented in Fig. 35. For the EN 1993-1-6 strength curve, the relative buckling strength χ is a function of the relative slenderness $\bar{\lambda}_c$ and meridional buckling parameters (α, β, η and $\bar{\lambda}_p$) that are associated with the diameter-to-thickness ratios D/t of the reference circular shells. Four strength curves for Aster shells with various reference diameter-to-thickness ratios (i.e. A150×1.0, A180×1.0, A180×0.7 and A200×0.7, colored in black, blue, grey and purple, respectively) are plotted in Fig. 35. When the relative slenderness is determined based on E_0 (Fig. 35(a)), the Aster shell test and FE results lie generally above the EN 1993-1-6 strength curve owing to their improved post-buckling stability relative to their circular counterparts, but below the EN 1993-1-4 strength curve for plated elements. There are, however, a small number of Aster shells of medium slenderness, which exhibited behavior more akin to cylindrical shells, that fall below the EN 1993-1-6 strength curve. The reference circular shell FE results also lie below the EN 1993-1-6 strength curve. When the relative slenderness is determined based on E_{sec} (Fig. 35(b)), the Aster shell test and FE results lie well above the EN 1993-1-6 strength curve, and even generally above the EN 1993-1-4 strength curve for plated elements; the reference circular shell FE results also lie above the EN 1993-1-6 strength curve.

The mean ratios of the experimental and numerical ultimate loads N_u to the EN 1993-1-6 (CEN 2017) resistance predictions (denoted by $N_u/N_{u,EC3}$) along with the coefficient of variation

(COV), considering both the initial and secant moduli, E_0 and E_{sec}, are reported in Table 13. A value of $N_u/N_{u,EC3}$ greater than unity indicates a safe-sided resistance prediction. It can be seen that the EN 1993-1-6 (CEN 2017) strength predictions for the Aster and wavy shells are safe-sided on average, with use of the initial modulus E_0 rather than the secant modulus at the 0.2% proof stress E_{sec} yielding more accurate and less scattered results. Note that the test ultimate load of the circular cylindrical shell is overestimated by the design provisions using E_0 with $N_{u,test}/N_{u,pred}$=0.96, similar to other cylindrical shells of medium slenderness from the numerical study. Overall, it can be concluded that the design provisions of EN 1993-1-6 can be applied to optimized stainless steel Aster and free-form wavy shells produced by PBF under axial compression, though further research is required to determine suitable safety factors.

5. Conclusions

This paper presents an experimental and numerical study into the structural behavior of stainless steel circular and corrugated cylindrical shells subjected to axial compression. One circular, three Aster and six wavy cylindrical shells were additively manufactured by powder bed fusion (PBF) using 316L and CX stainless steel powders. 3D laser-scanning and digital image correlation (DIC) techniques were employed for the capture of the geometries and deformation fields of the test specimens, respectively. The test setup, test procedure and key test outputs of the compression tests are fully described. The circular cylindrical shell buckled in a chequerboard pattern with a sudden drop in the applied load. The corrugated cylindrical shells exhibited axisymmetric deformation modes and failed by local buckling in the troughs of the corrugations, with substantially higher failure stresses than their reference circular cylindrical shell.

Following the experimental program, shell FE models were established, validated against the test results and then employed in subsequent parametric studies to expand the current experimental database; a total of 2764 numerical cross-sectional resistance data over a wide range of diameter-to-thickness ratios, amplitudes and numbers of corrugations were generated for Aster shells. Finally, the combined set of experimental and numerical data was utilized to assess the applicability of existing design provisions, particularly those given in EN 1993-1-6 for shell structures, to the design of the examined corrugated cross-sections produced by PBF. Overall, the EN 1993-1-6 design rules are shown to provide safe-sided buckling resistance predictions for stainless steel PBF manufactured corrugated cross-sections.

Data Availability Statement

Some data for the PBF 316L stainless steel shells, models, or code that support the findings of this study are available from the corresponding author upon reasonable request.

Acknowledgments

The authors would like to acknowledge the contribution of the LUT Laser Laboratory for building the test specimens and the financial support from the China Scholarship Council. We are grateful to the copyright holder (Ernst & Sohn) for permission to reproduce part of the article, Zhang et al. "Optimisation and compressive testing of additively manufactured stainless steel corrugated shells" in Proceedings of 9th European Conference on Steel and Composite Structures (Eurosteel 2021).

References

Afkhami, S., V. Javaheri, E. Dabiri, H. Piili, and T. Björk. 2022. "Effects of manufacturing parameters, heat treatment, and machining on the physical and mechanical properties of 13Cr10Ni1.7Mo2Al0.4Mn0.4Si steel processed by laser powder bed fusion." *Materials Science and Engineering: A*, 832 (Jan): 142402.

Araar, M., M. Derbali, and J. F. Jullien. 1998. "Buckling of the multi-vaulted 'Aster' shell under axial compression alone or combined with an external pressure." *Structural Engineering and Mechanics*, 6 (7): 827–839.

Arrayago, I., E. Real, and L. Gardner. 2015. “Description of stress–strain curves for stainless steel alloys.” *Materials & Design*, 87 (Dec): 540–552.

Asgari, H., and M. Mohammadi. 2018. “Microstructure and mechanical properties of stainless steel CX manufactured by Direct Metal Laser Sintering.” *Materials Science and Engineering: A*, 709 (Jan): 82–89.

Ashraf, M., L. Gardner, and D. A. Nethercot. 2006. “Compression strength of stainless steel cross-sections.” *Journal of Constructional Steel Research*, 62(1-2): 105–115.

CEN (European Committee for Standardization). 2006. *Eurocode 3 - Design of steel structures - Part 1-5: Plated structural elements*. EN 1993-1-5:2006. Brussels, Belgium: CEN.

CEN (European Committee for Standardization). 2015. *Eurocode 3-Design of steel structures. Part 1-4: General rules-Supplementary rules for stainless steels*. EN 1993-1-4:2006+A1:2015. Brussels, Belgium: CEN.

CEN (European Committee for Standardization). 2016. *Metallic materials — Tensile testing Part 1: Method of test at room temperature*. EN ISO 6892-1. Brussels, Belgium: CEN.

CEN (European Committee for Standardization). 2017. *Eurocode 3 - Design of steel structures, Part 1-6: Strength and Stability of Shell Structures*. EN 1993-1-6:2007+A1:2017. Brussels, Belgium: CEN.

Centre for Advanced Structural Engineering. 1990. *Compression tests of stainless steel tubular columns*. Sydney, Australia.

Combescure, A., and J. F. Jullien. 2015. “ASTER Shell: a simple concept to significantly increase the plastic buckling strength of short cylinders subjected to combined external pressure and axial compression.” *Advanced Modeling and Simulation in Engineering Sciences*, 2 (1), 1-27.

EOS. 2017. “EOS Stainless Steel 316L Material Data Sheet.”

EOS. 2019. “EOS Stainless Steel CX Material Data Sheet.”

Gardner, L. Submitted. “Metal additive manufacturing in structural engineering – review, advances, opportunities and outlook.” *Structures*.

Gardner, L., and M. Ashraf. 2006. “Structural design for non-linear metallic materials.” *Engineering Structures,* 28 (6): 926–934.

Gardner, L., and M. Theofanous. 2008. “Discrete and continuous treatment of local buckling in stainless steel elements.” *Journal of Constructional Steel Research*, 64(11): 1207-1216.

Gardner, L., and X. Yun. 2018. “Description of stress-strain curves for cold-formed steels.” *Construction and Building Materials*, 189 (Nov): 527–538.

Hilburger, M. W., M. P. Nemeth, and J. H. Starnes. 2006. “Shell buckling design criteria based on manufacturing imperfection signatures.” *AIAA Journal*, 44 (3): 654–663.

Huang, C., P. Kyvelou, R. Zhang, T. B. Britton, and L. Gardner. 2022. “Mechanical testing and microstructural analysis of wire arc additively manufactured steels.” *Materials & Design*, 216 (Apr): 110544.

Hutchinson, J. W., and J. C. Frauenthal. 1969. “Elastic Postbuckling Behavior of Stiffened an Barreled Cylindrical Shells.” *Journal of Applied Mechanics,* 36 (4): 784–790.

Kanyilmaz, A., A.G. Demir, M. Chierici, F. Berto, L. Gardner, S.Y. Kandukuri, P. Kassabian, T. Kinoshita, A. Laurenti, I. Paoletti, and A. Du Plessis. 2021. “Role of metal 3D printing to increase quality and resource-efficiency in the construction sector.” *Additive Manufacturing*, 50 (Feb): 102541.

Kianersi, D., A. Mostafaei, and A. A. Amadeh. 2014. “Resistance spot welding joints of AISI 316L austenitic stainless steel sheets: Phase transformations, mechanical properties and microstructure characterizations.” *Materials & Design*, 61 (Sep): 251–263.

Knapp, R. H. 1977. “Pseudo-Cylindrical Shells: a New Concept for Undersea Structures.” *Journal of Engineering for Industry,* 99 (2): 485–492.

Meng, X., and L. Gardner. 2020a. “Testing of hot-finished high strength steel SHS and RHS under combined compression and bending.” *Thin-Walled Structures*, 148 (Mar): 106262.

Meng, X., and L. Gardner. 2020b. “Cross-sectional behaviour of cold-formed high strength steel circular hollow sections.” *Thin-Walled Structures*, 156 (Nov): 106822.

Meng, X., L. Gardner, A. J. Sadowski, and J. M. Rotter. 2020. “Elasto-plastic behaviour and design of semi-compact circular hollow sections.” *Thin-Walled Structures*, 148 (Mar): 106486.

Mirambell, E., and E. Real. 2000. “On the calculation of deflections in structural stainless steel beams: An experimental and numerical investigation.” *Journal of Constructional Steel Research*, 54 (1): 109–133.

NASA (National Aeronautics and Space Administration). 1968. *Bucking of Thin-Walled Circular Cylinders*. NASA SP-8007. Washington, D.C.: NASA.

NASA (National Aeronautics and Space Administration). 2020. *Buckling of thin-walled circular cylinders*. NASA SP-8007. 2nd ed. Washington, D.C.: NASA.

Niloufari, A., H. Showkati, M. Maali, and S. M. Fatemi. 2014. “Experimental investigation on the effect of geometric imperfections on the buckling and post-buckling behavior of steel tanks under hydrostatic pressure.” *Thin-Walled Structures*, 74 (Jan): 59–69.

Ning, X., and S. Pellegrino. 2015. “Imperfection-insensitive axially loaded thin cylindrical shells.” *International Journal of Solids and Structures*, 62 (Jun): 39–51.

Ning, X., and S. Pellegrino. 2017. “Experiments on imperfection insensitive axially loaded cylindrical shells.” *International Journal of Solids and Structures*, 115–116 (Jun): 73–86.

Ramberg, W., and W. R. Osgood. 1943. *Description of stress-strain curves by three parameters*. Technical Note, No. 902. Washington, D.C., USA: NACA (National Advisory Committee for Aeronautics).

Rasmussen, K. J. R. 2003. “Full-range stress–strain curves for stainless steel alloys.” *Journal of Constructional Steel Research*, 59 (1): 47–61.

Reitinger, R., K. U. Bletzinger, and E. Ramm. 1994. “Shape optimization of buckling sensitive structures.” *Computing Systems in Engineering*, 5 (1): 65–75.

Reitinger, R., and E. Ramm. 1995. “Buckling and imperfection sensitivity in the optimization of shell structures.” *Thin-Walled Structures*, 23 (1-4): 159–177.

Sanjari, M., A. Hadadzadeh, H. Pirgazi, A. Shahriari, B. S. Amirkhiz, L. A. I. Kestens, and M. Mohammadi. 2020. “Selective laser melted stainless steel CX: Role of built orientation on microstructure and micro-mechanical properties.” *Materials Science and Engineering: A*, 786 (Jun): 139365.

Schafer, B. W., M. Grigoriu, and T. Peköz. 1996. “A Probabilistic Examination of the Ultimate Strength of Cold- formed Steel Elements.” In *Proceedings of 13th International Specialty Conference on Cold-Formed Steel Structures*, Missouri, USA.

Schafer, B. W., and T. Peköz. 1998. “Computational modeling of cold-formed steel: characterizing geometric imperfections and residual stresses.” *Journal of Constructional Steel Research*, 47 (3): 193–210.

Singer, J., J. Arbocz, and C. D. Babcock. 1971. “Buckling of imperfect stiffened cylindrical shells under axial compression.” *AIAA Journal*, 9 (1): 68–75.

Teng, J. G., X. Lin, J. M. Rotter, and X. L. Ding. 2005. “Analysis of geometric imperfections in full-scale welded steel silos.” *Engineering Structures*, 27 (6): 938–950.

Wagner, H. N. R., C. Hühne, K. Rohwer, S. Niemann, and M. Wiedemann. 2017. “Stimulating the realistic worst case buckling scenario of axially compressed unstiffened cylindrical composite shells.” *Composite Structures*, 160 (Jan): 1095–1104.

Weingarten, V. I., E. J. Morgan, and P. Seide. 1965. “Elastic stability of thin-walled cylindrical and conical shells under axial compression.” *AIAA Journal*, 3 (3): 500–505.

Ye, J., P. Kyvelou, F. Gilardi, H. Lu, M. Gilbert, and L. Gardner. 2021. “An end-to-end framework for the additive manufacture of optimized tubular structures.” *IEEE Access*, 9: 165476-165489.

Yoshimura, Y. 1955. *On the mechanism of buckling of a circular cylindrical shell under axial compression*. Technical Report, No. NACA-TM-1390. Washington, D.C., USA: NACA (National Advisory Committee for Aeronautics).

Yu, C., and B. Schafer. 2005. *Distortional Buckling of Cold-formed Steel members in Bending*. Final Report, Maryland, USA: AISI (American Iron and Steel Institute).

Yuan, H. X., Y. Q. Wang, Y. J. Shi, and L. Gardner. 2014. “Stub column tests on stainless steel built-up sections.” *Thin-Walled Structures*, 83 (Oct):103-114.

Yun, X., L. Gardner, and N. Boissonnade. 2018. “Ultimate capacity of I-sections under combined loading – Part 1: Experiments and FE model validation.” *Journal of Constructional Steel Research*, 147 (Aug): 408-421.

Yun, X., Z. Wang, and L. Gardner. 2021. “Full-Range Stress–Strain Curves for Aluminum Alloys.” *Journal of Structural Engineering*, 147 (6): 04021060.

Zhang, R., L. Gardner, M. Amraei, and H. Piili. Submitted. “Microstructure, mechanical properties and cross-sectional behaviour of additively manufactured stainless steel cylindrical shells.” *Thin-Walled Structures*.

Zhang, R., L. Gardner, C. Buchanan, V. P. Matilainen, H. Piili, and A. Salminen. 2021a. “Testing and analysis of additively manufactured stainless steel CHS in compression.” *Thin-Walled Structures*, 159 (Feb): 107270.

Zhang, R., L. Gardner, X. Meng, C. Buchanan, V. Matilainen, H. Piili, and A. Salminen. 2021b. “Optimisation and compressive testing of additively manufactured stainless steel corrugated shells.” In *Proceedings of 9th European Conference on Steel and Composite*

Structures (Eurosteel 2021), Sheffield, UK. © 2021 Ernst & Sohn Verlag für Architektur und technische Wissenschaften GmbH & Co. KG.

Zhang, R., X. Meng, and L. Gardner. 2022. “Shape optimisation of stainless steel corrugated cylindrical shells for additive manufacturing.” *Engineering Structures*, 270 (Nov): 114857.

Zhang, Z., G. Shi, L. Hou, and L. Zhou. 2021c. “Geometric dimension and imperfection measurements of box-T section columns using 3D scanning.” *Journal of Constructional Steel Research*, 183 (Aug): 106742.

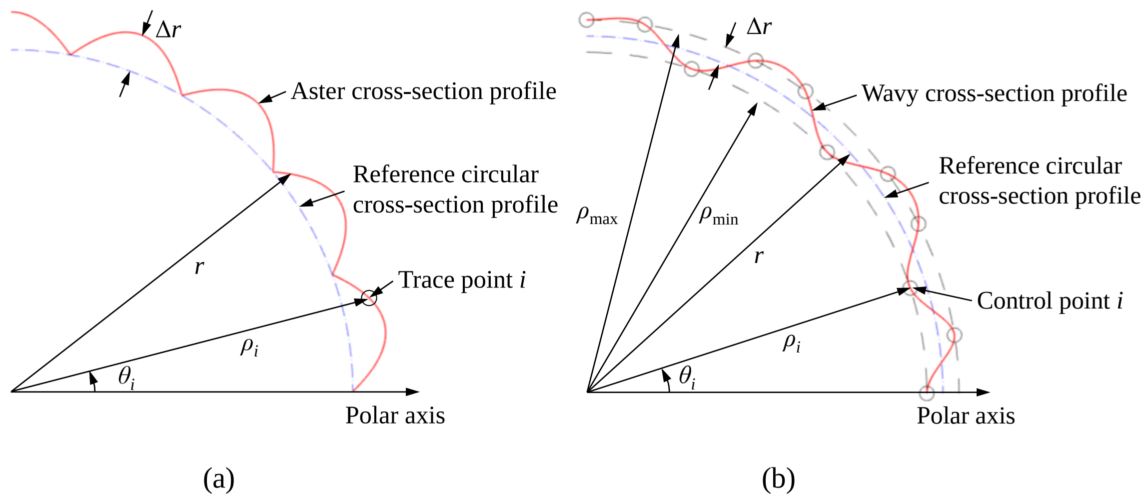

Fig. 1 One quarter of (a) Aster and (b) wavy cross-section profiles, showing points lying on the curves and reference circular cross-section profile

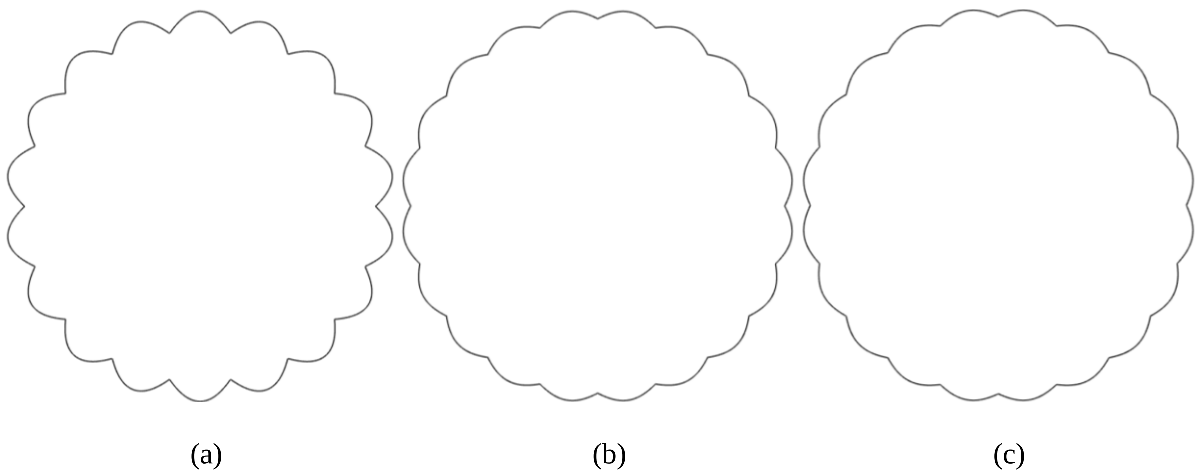

Fig. 2 Cross-section profiles of printed Aster shells: (a) A200×1.0, (b) A180×0.7 and (c) A200×0.7

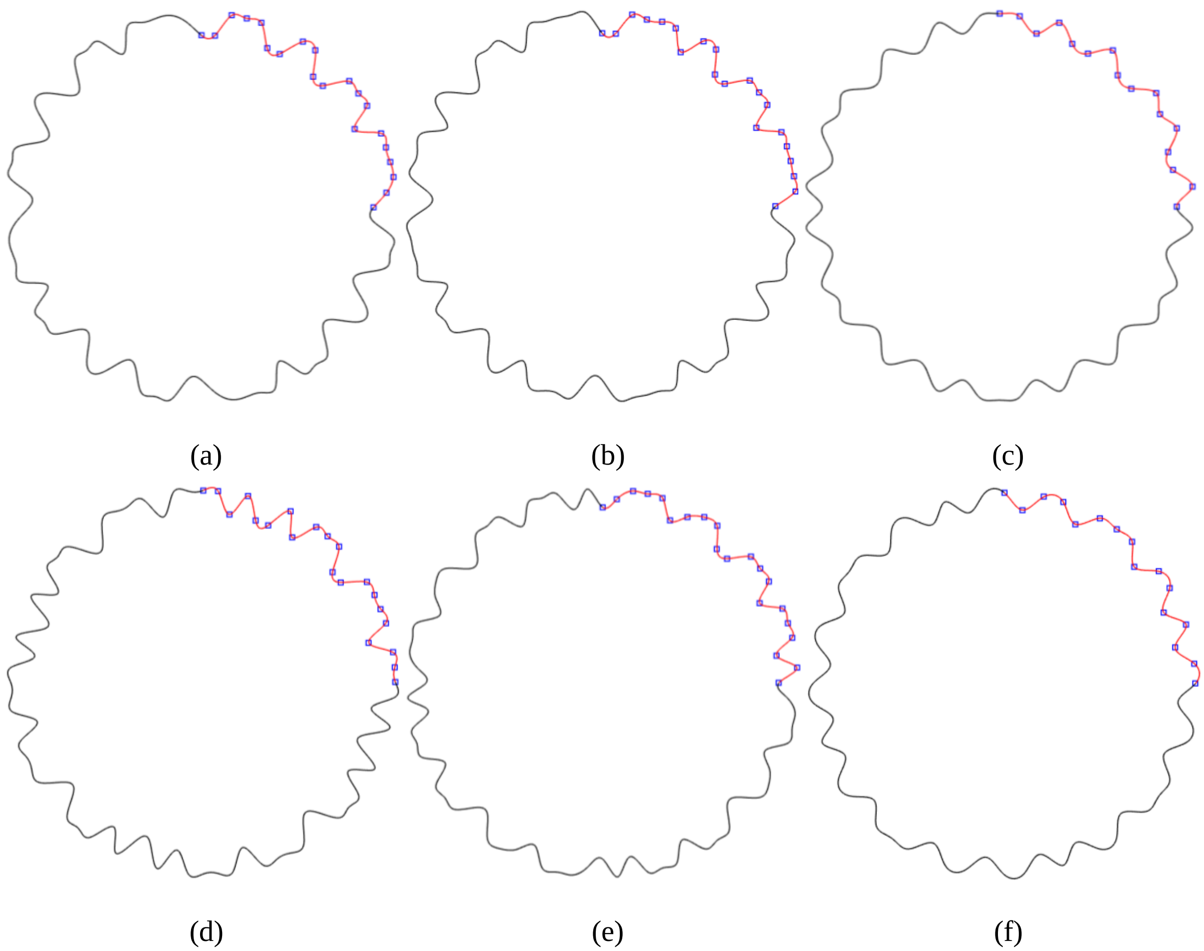

Fig. 3 Cross-section profiles of printed wavy cylindrical shells: (a) W150×1.0, (b) W180×1.0, (c) W200×1.0, (d) W150×0.7, (e) W180×0.7 and (f) W200×0.7

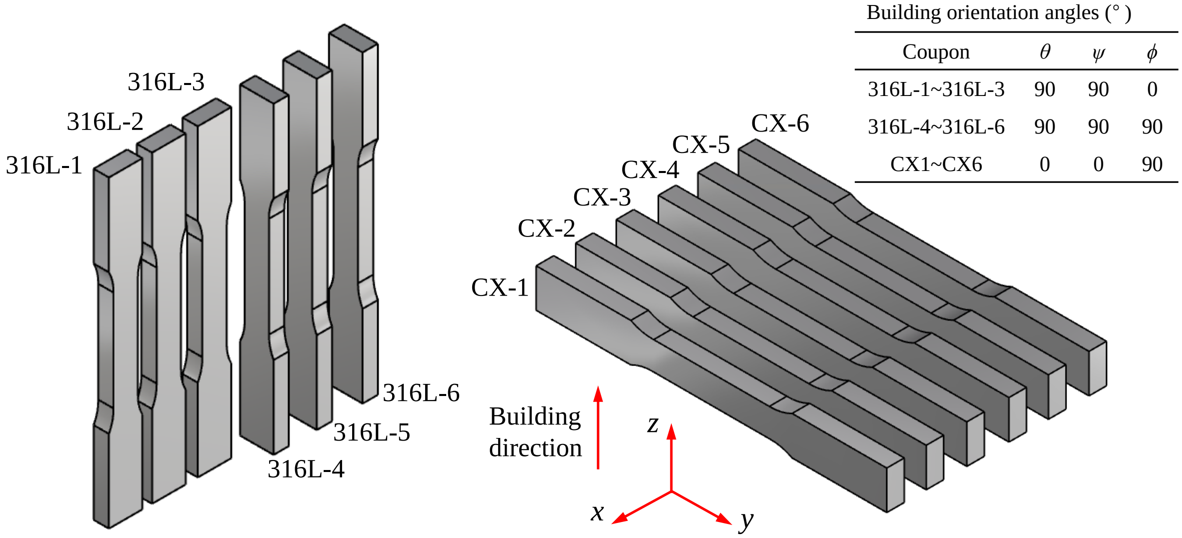

Building orientation angles (°)

Coupon	θ	ψ	ϕ
316L-1~316L-3	90	90	0
316L-4~316L-6	90	90	90
CX1~CX6	0	0	90

Fig. 4 Schematic of test coupons, showing the building orientation angles

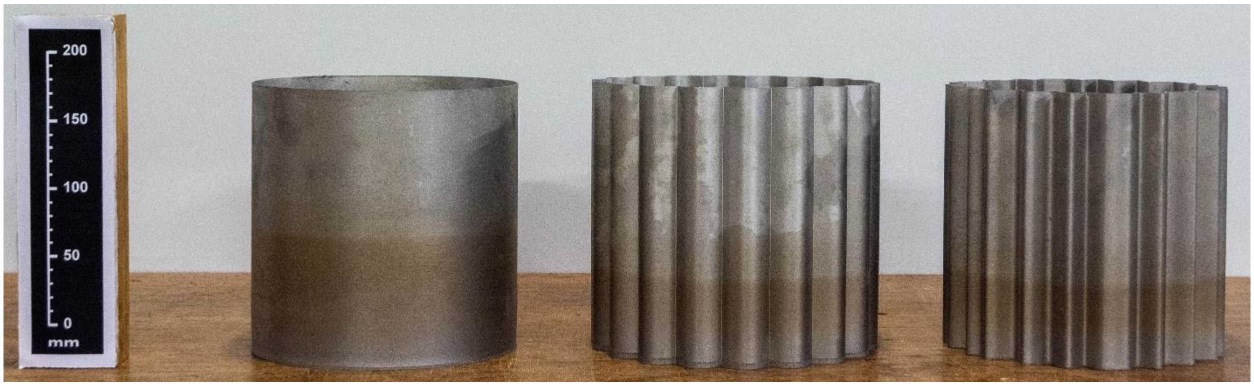

Fig. 5 Photograph of three types of PBF shell specimens (from left to right: circular, Aster and wavy)

(a)

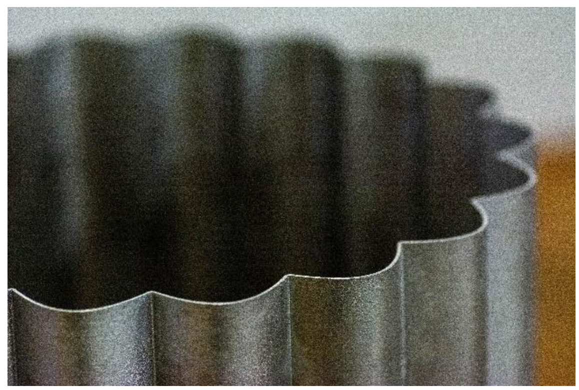

(b)

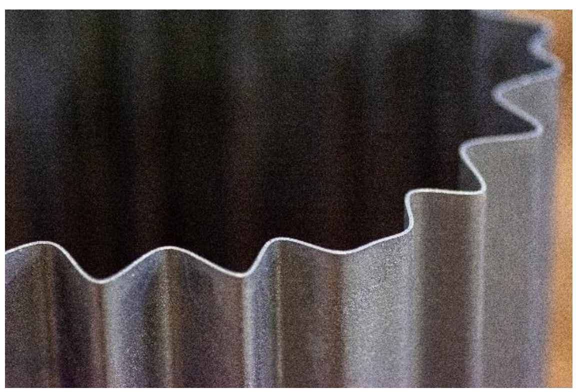

(c)

Fig. 6 Close-up view of typical PBF (a) circular, (b) Aster and (c) wavy cylindrical shells

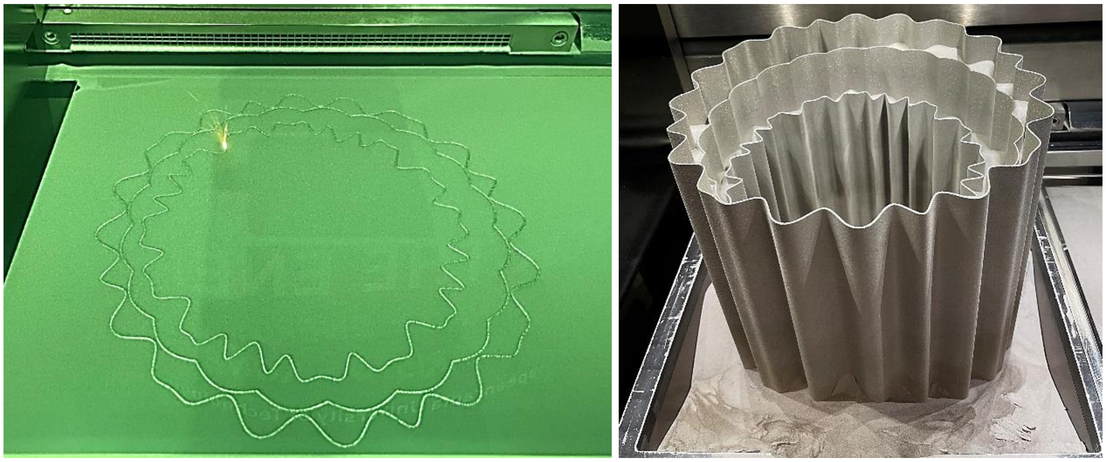

Fig. 7 Shell specimens (a) during and (b) after printing

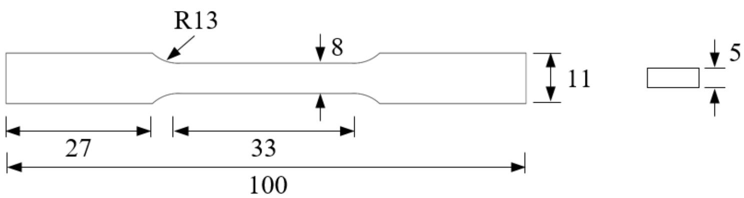

Fig. 8 Dimensions of tensile coupons (unit: mm)

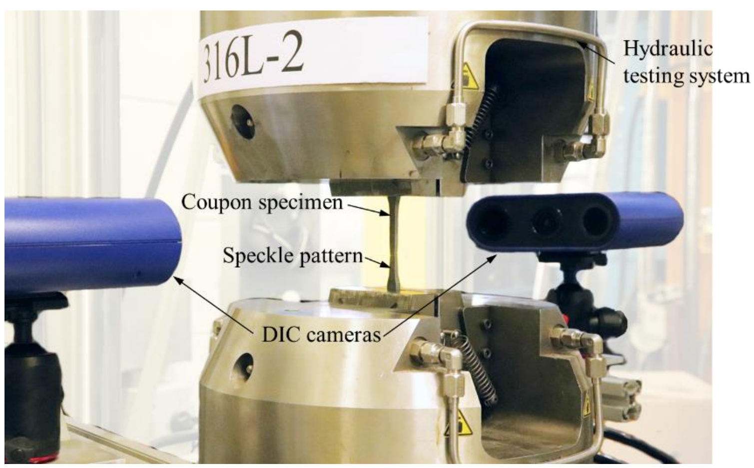

Fig. 9 Tensile coupon test setup with 3D stereo-DIC system

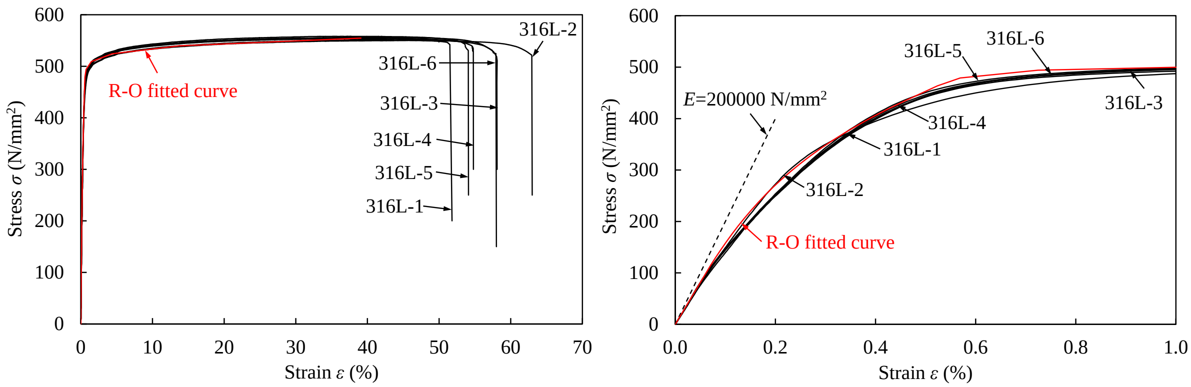

(a) (b)

Fig. 10 Stress-strain curves of PBF 316L stainless steel tensile coupons for the (a) full range and (b) initial range

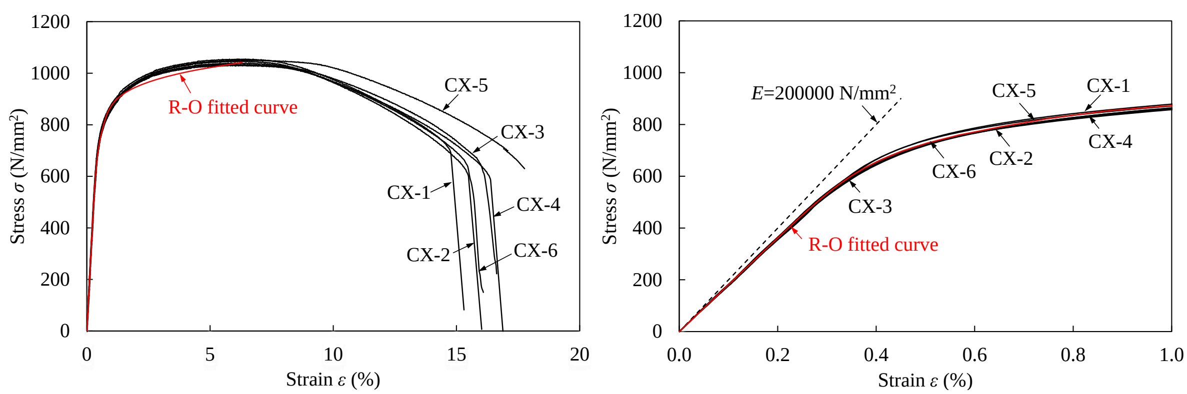

(a) (b)

Fig. 11 Stress-strain curves of PBF CX stainless steel tensile coupons for the (a) full range and (b) initial range

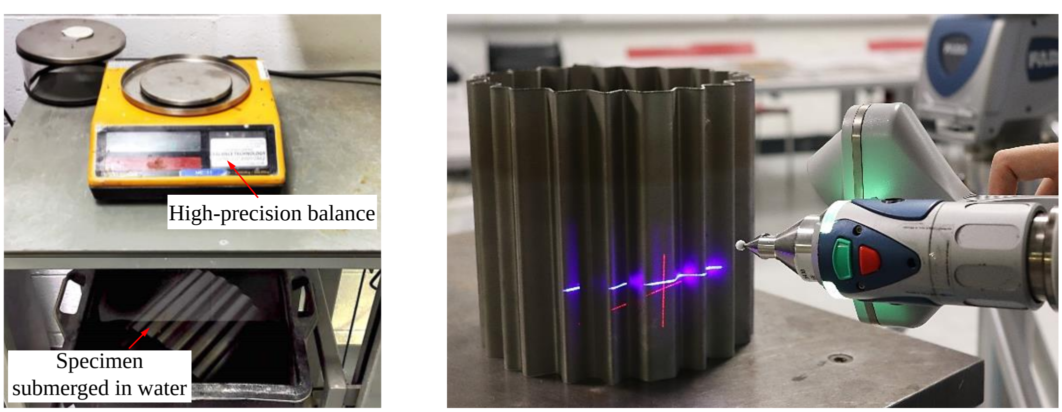

(a) (b)

Fig. 12 Setup for geometric measurements: (a) Archimedes' method and (b) laser scanning

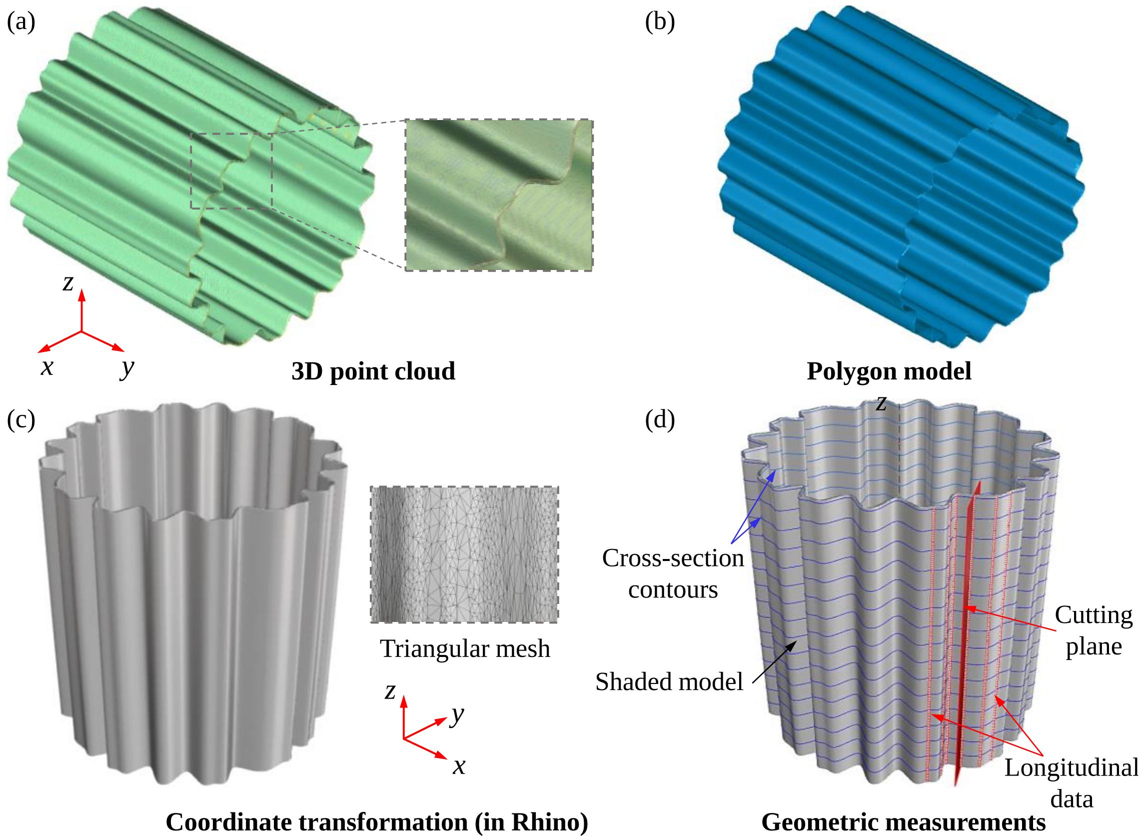

Fig. 13 Schematic diagram of geometric measurements based on 3D laser-scanning: (a) 3D point cloud, (b) polygon model, (c) coordinate transformation and (d) extraction of cross-section profiles and longitudinal points

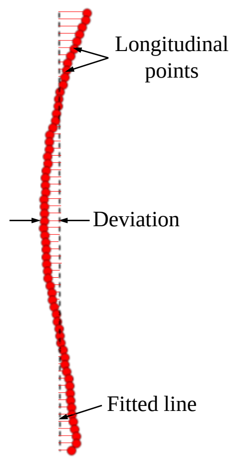

Fig. 14 Schematic showing determination of longitudinal imperfection values

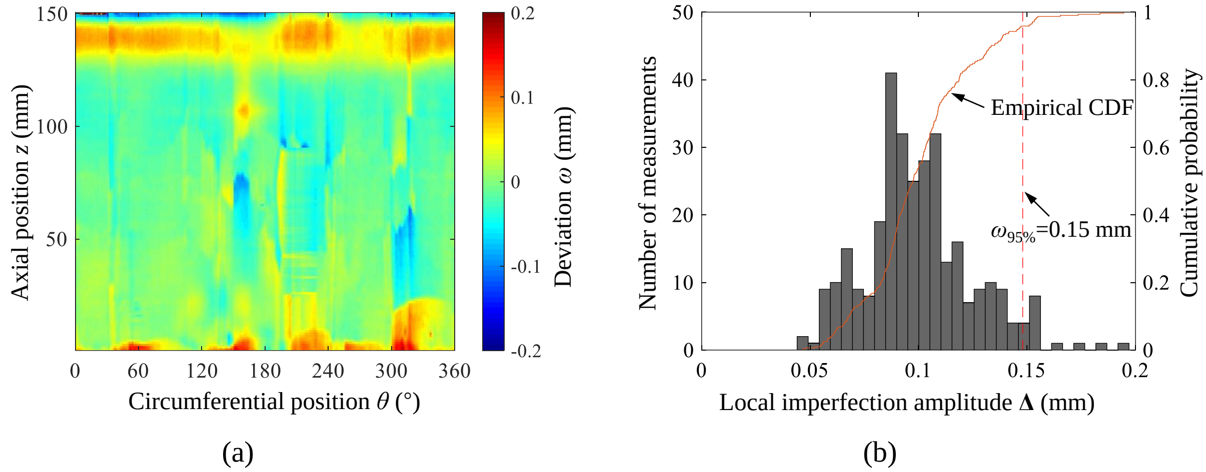

Fig. 15 (a) Measured imperfection distribution and (b) histogram and CDFs of longitudinal imperfections in the C200×1.0 circular cylindrical shell specimen

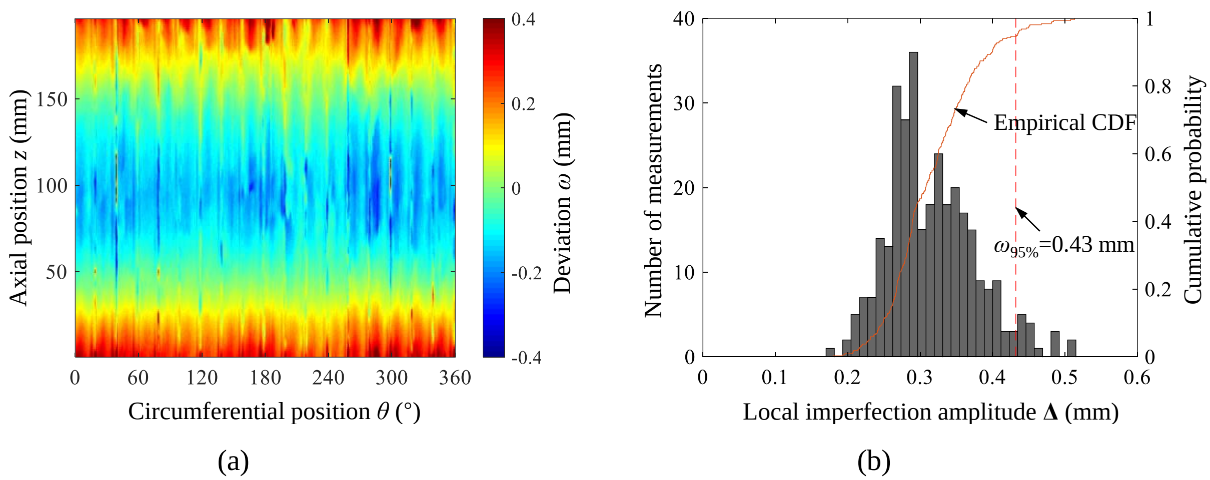

Fig. 16 (a) Measured imperfection distribution and (b) histogram and CDFs of longitudinal imperfections in the A200×1.0 Aster shell specimen

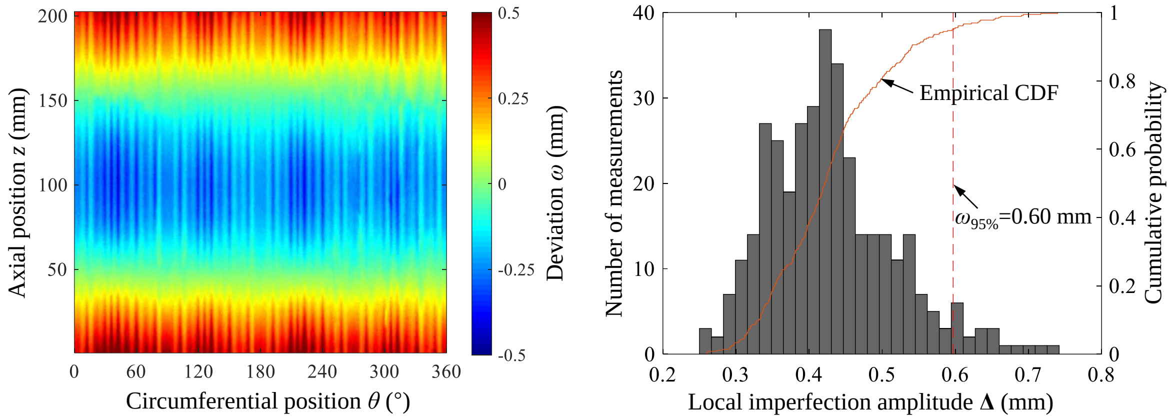

(a) (b)

Fig. 17 (a) Measured imperfection distribution and (b) histogram and CDFs of longitudinal imperfections in the W200×0.7 wavy cylindrical shell specimen

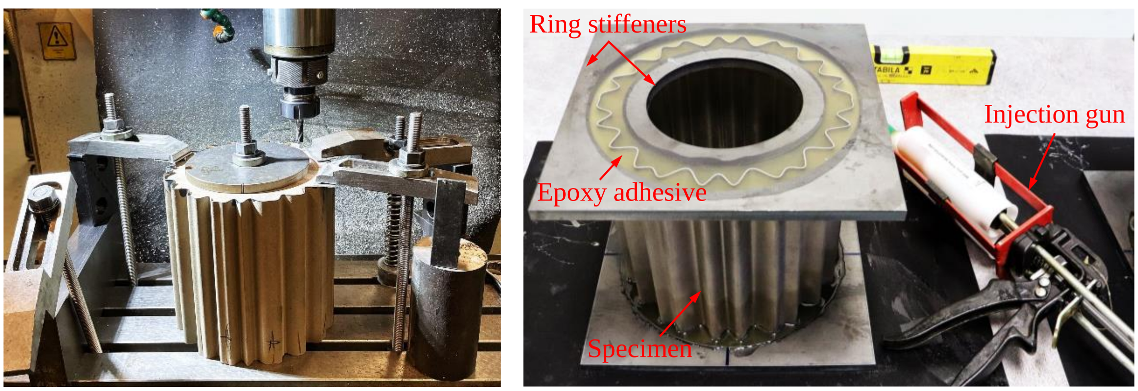

(a) (b)

Fig. 18 Shell specimen preparation for testing: (a) end machining and (b) potting

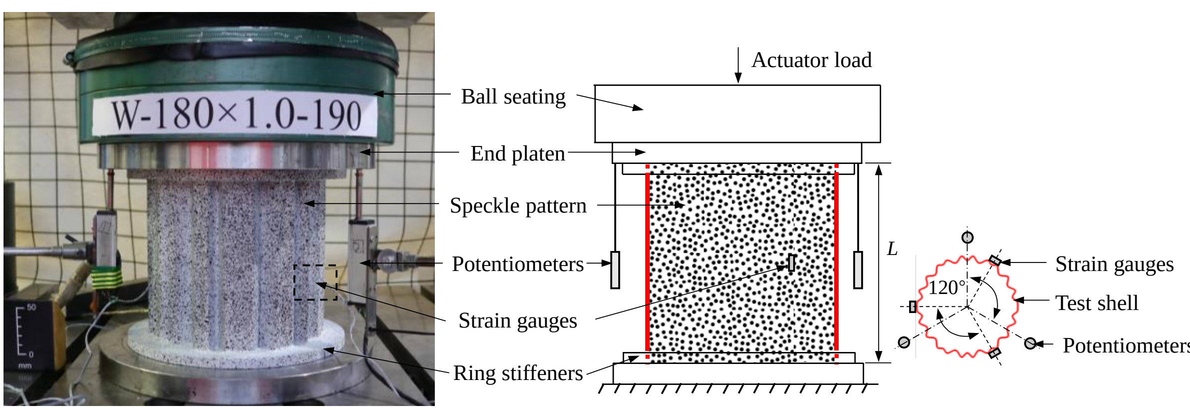

Fig. 19 Experimental configuration for shell compression tests

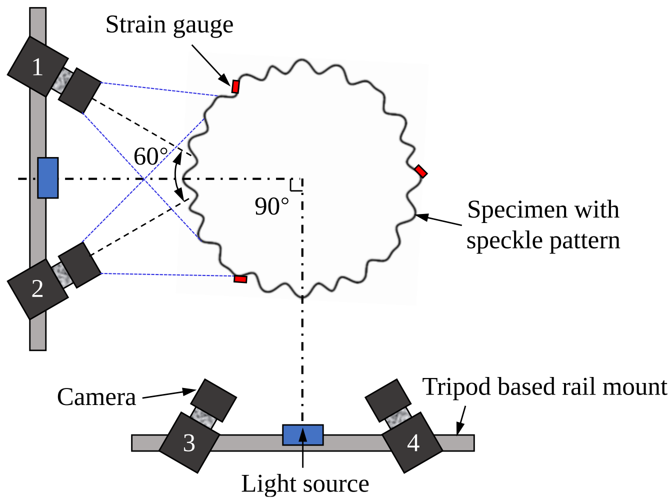

Fig. 20 Plan view of DIC system layout

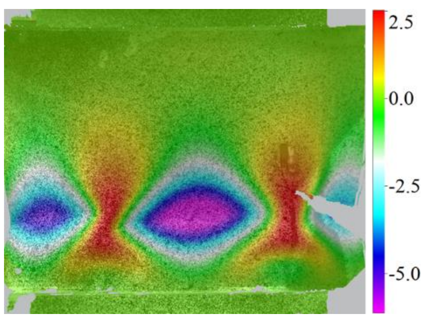

Fig. 21 Post-ultimate out-of-plane deformations (unit: mm) of circular cylindrical shell C200×1.0

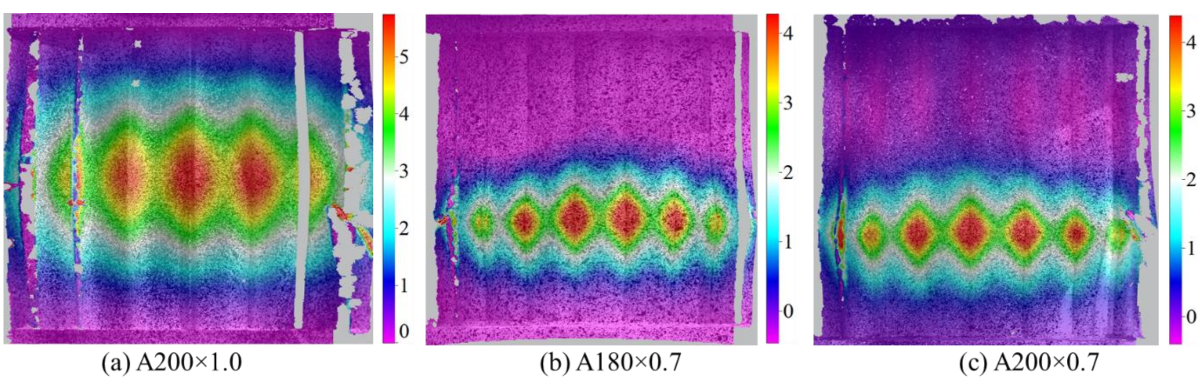

Fig. 22 Post-ultimate out-of-plane deformations (unit: mm) of Aster shells (a) A200×1.0, (b) A180×0.7 and (c) A200×0.7

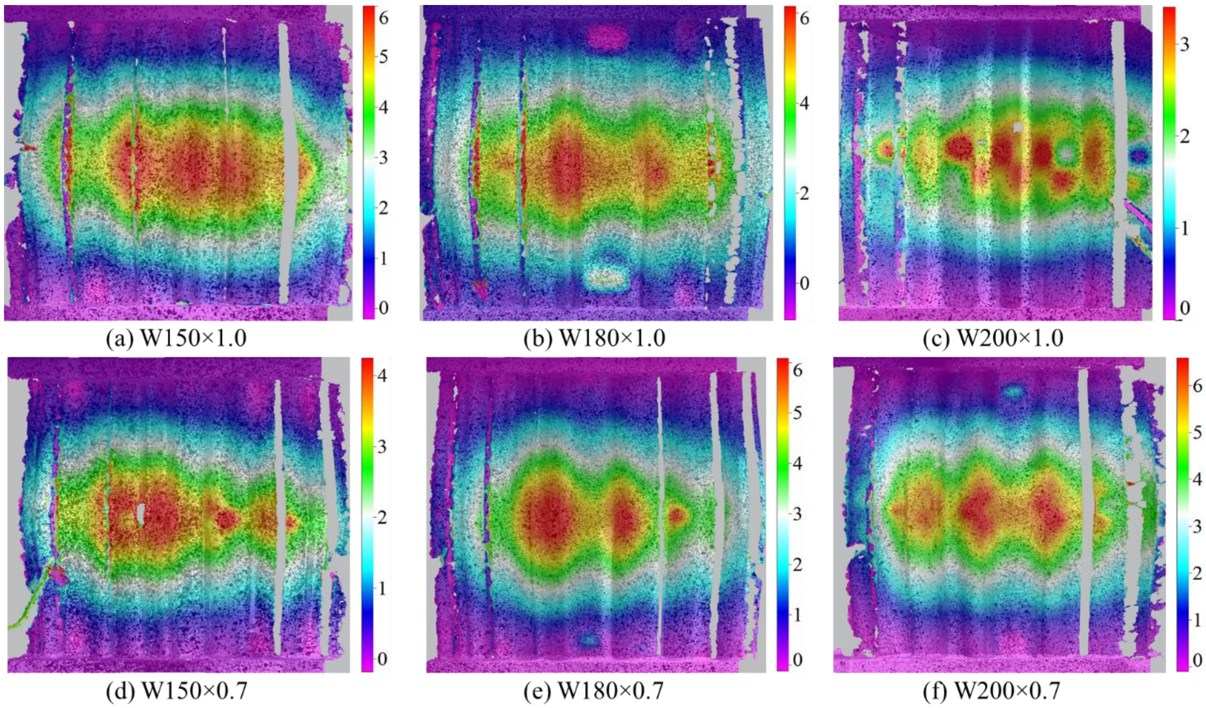

Fig. 23 Post-ultimate out-of-plane deformations (unit: mm) of wavy cylindrical shells (a) W150×1.0, (b) W180×1.0, (c) W200×1.0, (d) W150×0.7, (e) W180×0.7 and (f) W200×0.7

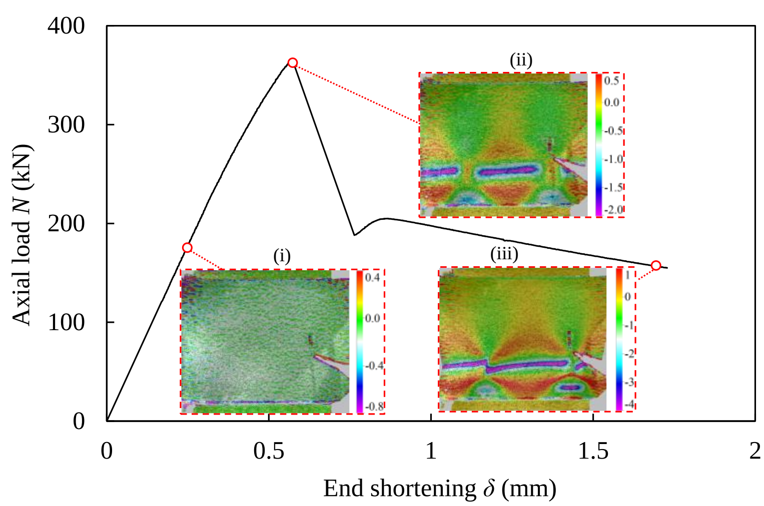

Fig. 24 Axial load end-shortening curve and DIC results from C200×1.0 compression test, showing axial strain distributions (unit: %) (i) at $0.5N_u$, (ii) just after N_u and (iii) when unloading

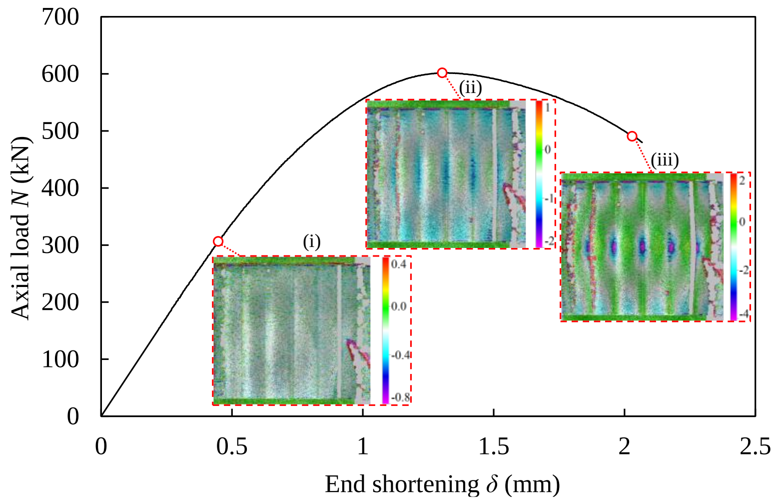

Fig. 25 Axial load end-shortening curve and DIC results from A200 ×1.0 compression test, showing axial strain distributions (unit: %) at (i) $0.5N_u$, (ii) N_u and (iii) when unloading

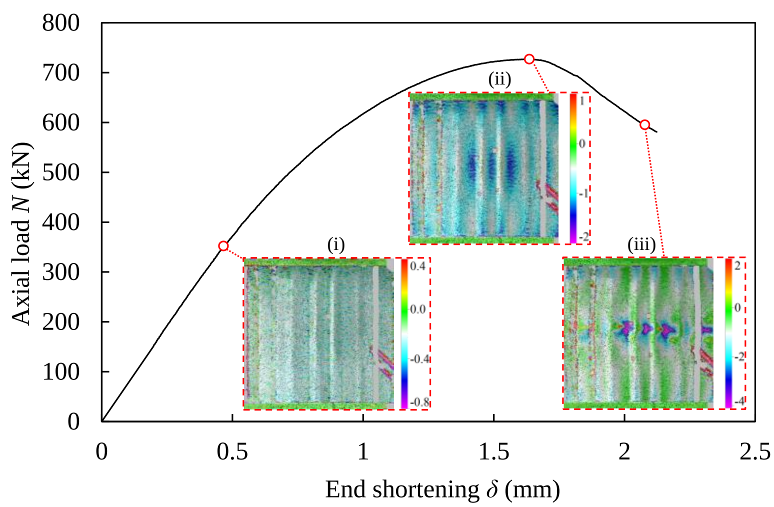

Fig. 26 Axial load end-shortening curve and DIC results from W200×1.0 compression tests, showing axial strain distributions (unit: %) at (i) $0.5N_u$, (ii) N_u and (iii) when unloading

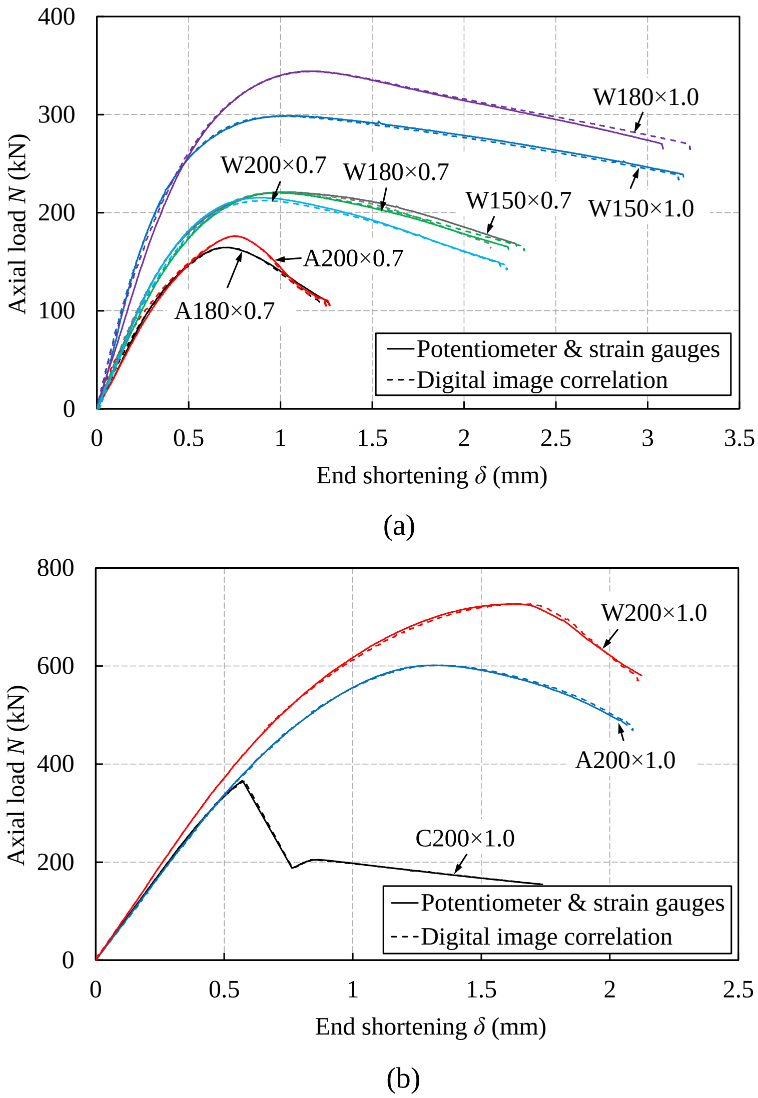

Fig. 27 Measured axial load end-shortening curves for the tested (a) 316L and (b) CX stainless steel shells

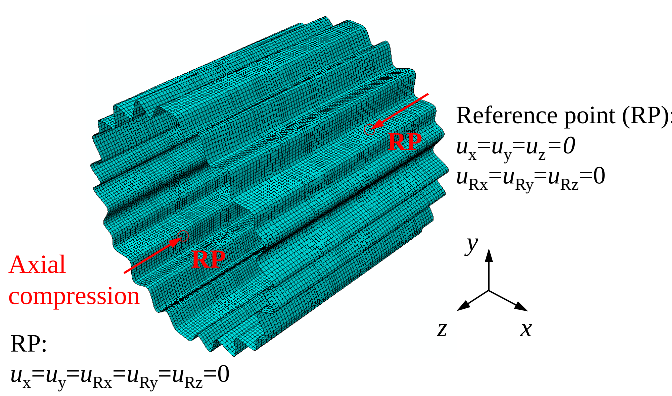

Fig. 28 Geometry, loading and boundary conditions of FE models for cylinders

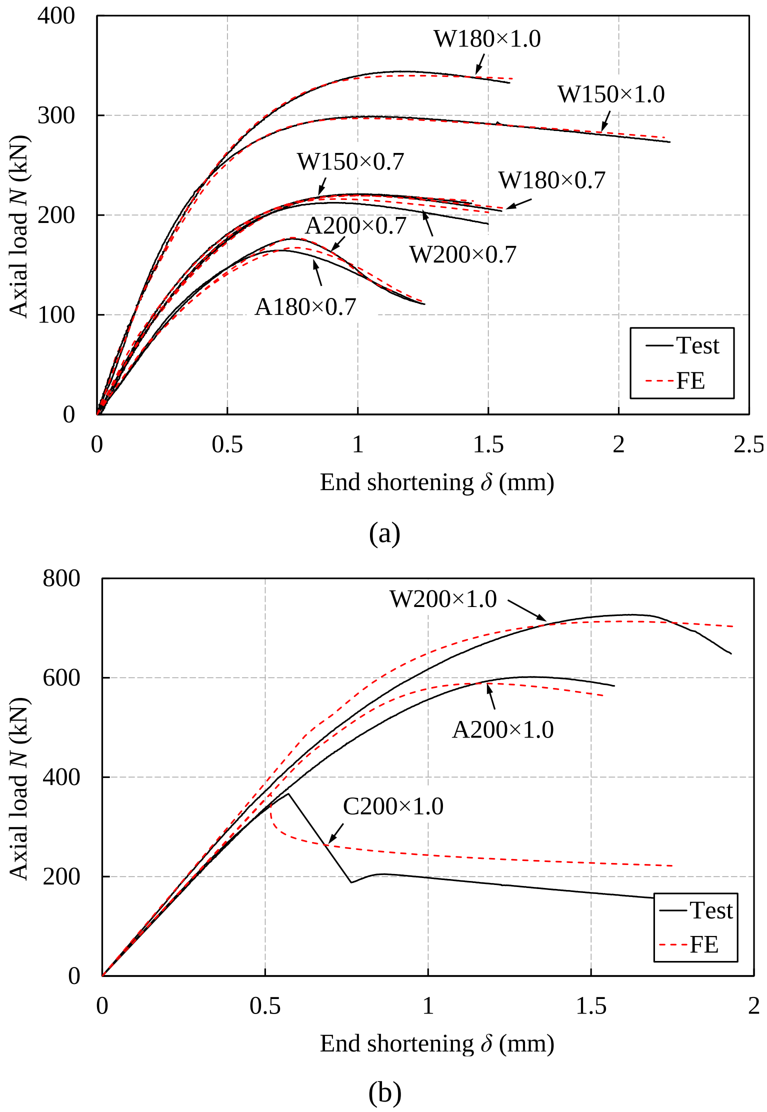

Fig. 29 Experimental and numerical load-deformation curves for axially compressed shells made from (a) 316L and (b) CX stainless steels, with numerical data derived based on scanned geometries

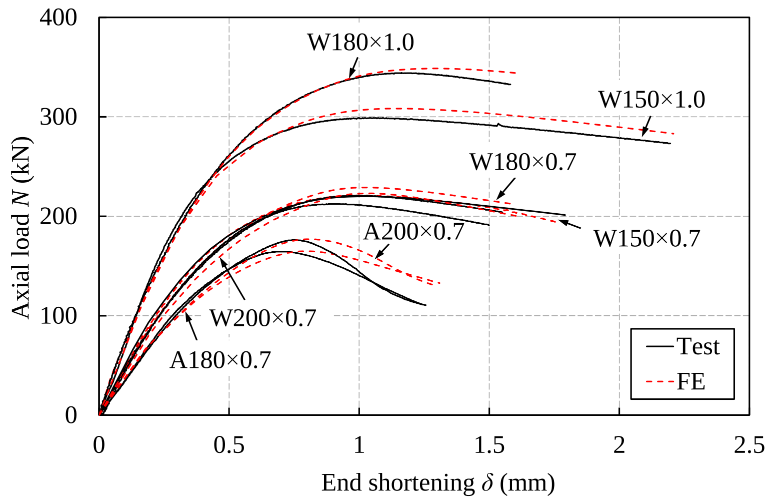

Fig. 30 Comparisons of experimental load-deformation curves with the results from FE simulations using eigenmode-affine imperfections for 316L stainless steel shells

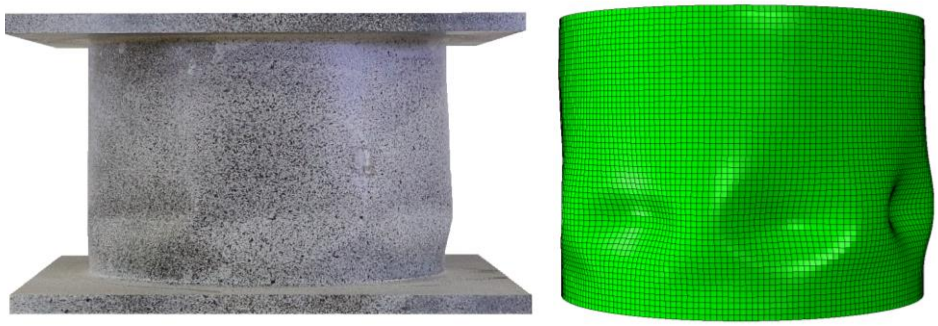

(a)

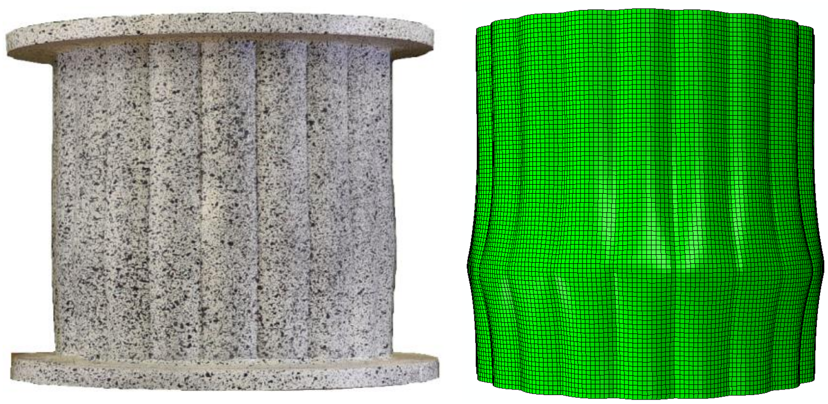

(b)

(c)

Fig. 31 Typical experimental and numerical failure modes of (a) circular, (b) Aster and (c) free-form wavy cylindrical shells, with numerical results derived based on eigenmode-affine imperfections

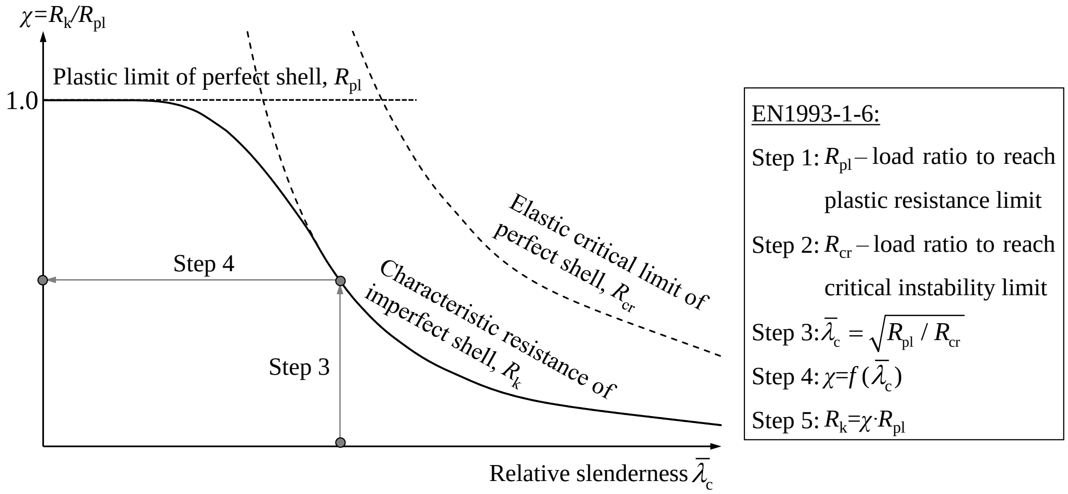

Fig. 32 Basic concept and procedure for buckling design specified in EN 1993-1-6 (CEN, 2017)

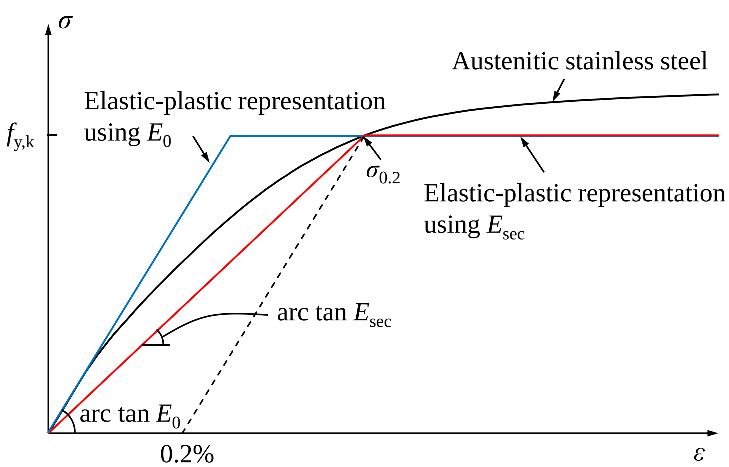

Fig. 33 Schematic stress-strain relationship for austenitic stainless steel and elastic-plastic models, with the characteristic yield strength $f_{y,k}$ taken equal to the 0.2% proof strength

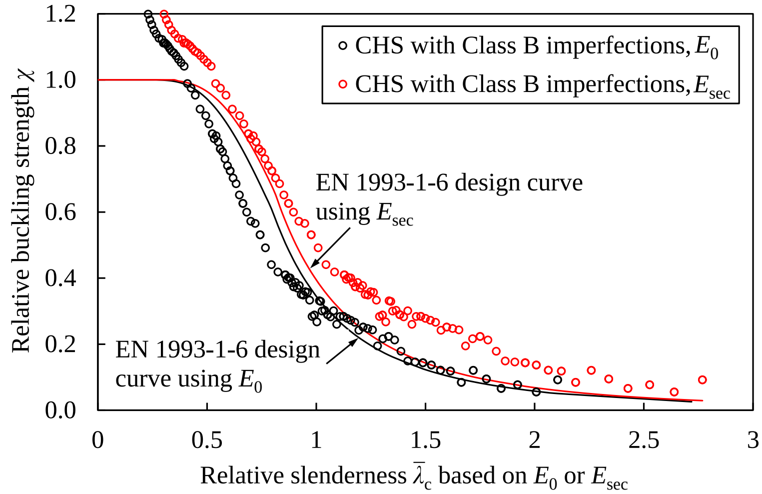

Fig. 34 Strength reduction factors for circular hollow sections using initial tangent modulus E_0 and secant modulus at the 0.2% proof stress E_{sec}

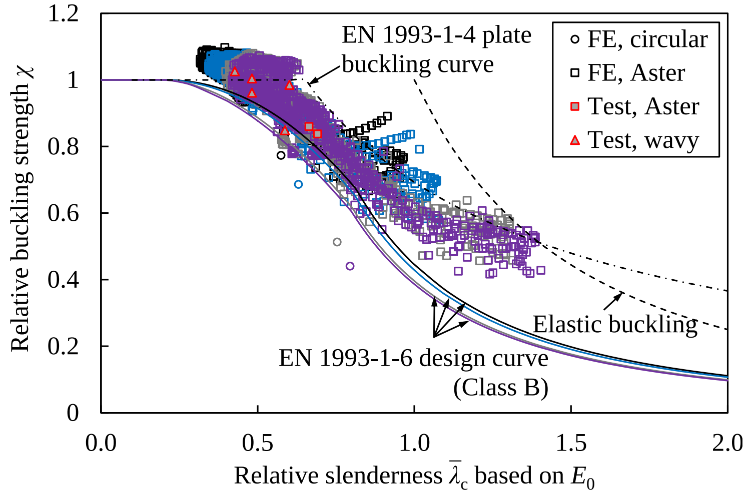

(a)

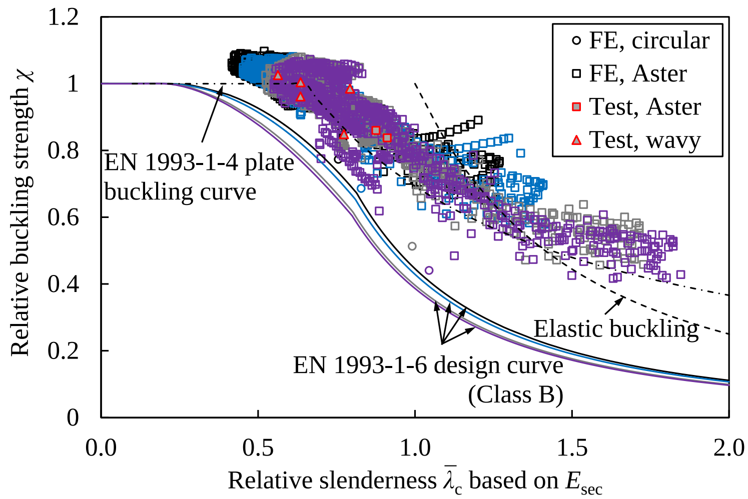

(b)

Fig. 35 Comparison of experimental and numerical buckling resistance with EN 1993-1-6 resistance predictions using (a) initial tangent modulus and (b) secant modulus at the 0.2% proof stress. The black, blue, grey and purple data points correspond to A150×1.0, A180×1.0, A180×0.7 and A200×0.7 Aster shells and their circular counterparts respectively.

Table 1 Nominal chemical composition of the employed EOS 316L and CX stainless steel powders, as provided by the manufacturer (EOS 2017, 2019)

Material	Cr (%)	Ni (%)	Mo (%)	Al (%)	C (%)	Mn (%)	Cu (%)	P (%)	S (%)	Si (%)	N (%)	Fe (%)
316L stainless steel	17.00-19.00	13.00-15.00	2.25-3.00	-	≤0.03	≤2.00	≤0.50	≤0.025	≤0.01	≤0.75	≤0.1	balance
CX stainless steel	11.00-13.00	8.40-10.00	1.10-1.70	1.20-2.00	≤0.05	≤0.40	-	-	-	≤0.40	-	balance

Table 2 Nominal material properties of parts built using the employed EOS stainless steel powders, as provided by the manufacturer (EOS 2017, 2019)

Material	Source	θ (°)	E (N/mm^2)	$\sigma_{0.2}$ (N/mm^2)	σ_u (N/mm^2)	ε_f (%)
316L stainless steel	As-built	0	185000	470-590	590-690	25-55
		90	180000	380-560	485-595	30-70
CX stainless steel	As-built	Average	-	840	1080	14

Table 3 Overview of the examined circular, Aster and wavy cylindrical shells, with nominal dimensions and parameters

Cross-section	Material	D (mm)	t (mm)	L (mm)	ω_a (mm)	Δr (mm)	M	Symmetry	N
C200×1.0	CX stainless steel	200	1.0	200	1.00	-	-	-	-
A200×1.0	CX stainless steel	200	1.0	200	1.00	11	18	-	-
A180×0.7	316L stainless steel	180	0.7	180	0.32	4.5	20	-	-
A200×0.7	316L stainless steel	200	0.7	200	0.33	4.5	20	-	-
W150×1.0	316L stainless steel	150	1.0	150	0.35	4.5	-	Rotational	21
W180×1.0	316L stainless steel	180	1.0	180	0.38	5.0	-	Rotational	21
W200×1.0	CX stainless steel	200	1.0	200	1.00	4.5	-	Mirror	16
W150×0.7	316L stainless steel	150	0.7	150	0.29	4.0	-	Rotational	21
W180×0.7	316L stainless steel	180	0.7	180	0.32	4.5	-	Rotational	21
W200×0.7	316L stainless steel	200	0.7	200	0.33	4.5	-	Rotational	16

Table 4 Radial deviations of control points of wavy shell designs, r_i-R (unit: mm)

Cross-section	1	2	3	4	5	6	7	8	9	10	11	12	13	14	15	16	17	18	19	20	21
W150×1.0	-4.50	1.02	4.50	4.50	4.50	4.50	-4.50	4.50	4.50	4.50	-4.50	-4.50	4.50	4.50	-4.50	-4.50	4.50	4.50	4.50	-4.50	4.50
W180×1.0	-5.00	5.00	5.00	5.00	5.00	5.00	-5.00	5.00	5.00	5.00	-5.00	-5.00	5.00	5.00	-5.00	4.50	5.00	4.06	5.00	-5.00	5.00
W200×1.0	-4.50	4.50	-4.50	-4.50	4.50	0.00	4.50	-4.50	-4.50	4.20	-4.50	-3.60	4.50	-4.50	3.30	4.20					
W150×0.7	4.35	4.35	4.35	-4.65	4.35	4.35	4.35	4.35	-4.65	-4.65	4.35	4.35	4.35	-4.65	4.35	-4.65	-4.65	4.35	-4.65	4.35	4.35
W180×0.7	-4.50	4.50	-4.50	4.50	4.50	4.50	-4.50	4.50	4.50	4.50	-4.50	-4.50	4.50	4.50	0.63	-4.50	4.50	4.47	4.50	-0.33	4.50
W200×0.7	4.50	4.50	-4.50	4.50	-4.50	4.50	4.50	-4.50	4.50	4.50	4.50	-4.50	4.50	4.50	-4.50	4.50					

Table 5 Optimization results of Aster and wavy cylindrical shells with various diameter-to-thickness ratios and results of their reference circular cylindrical shells

Cross-section	l_p (mm)	σ_{cr} (N/mm^2)	P_0 (kN)	min(P_+, P_-) (kN)	f_{ult} (N/mm^2)	γ	$\frac{f_{ult}}{\sigma_{0.2}}$	$\frac{f_{ult}}{f_{ult,cyl}}$
C150×1.0	468.1	1279.8	199.0	152.5	325.8	0.766	0.774	-
C180×1.0	562.3	1067.9	231.8	162.6	289.2	0.701	0.687	-
C200×1.0	625.2	1106.3	427.1	260.3	416.3	0.609	0.531	-
C150×0.7	469.0	895.0	130.1	81.7	248.8	0.628	0.591	-
C180×0.7	563.3	746.0	148.3	85.3	216.2	0.575	0.514	-
C200×0.7	626.1	672.2	158.8	80.5	183.7	0.507	0.436	-
A200×1.0	796.0	2283.4	613.5	606.5	761.9	0.989	0.972	1.831
A180×0.7	615.0	970.0	179.9	171.0	397.3	0.951	0.944	1.837
A200×0.7	674.7	861.6	192.9	180.7	382.5	0.937	0.909	2.085
W150×1.0	653.1	2247.4	298.2	296.9	454.7	0.996	1.080	1.395
W180×1.0	773.3	1048.1	350.2	346.3	447.9	0.989	1.064	1.549
W200×1.0	770.8	2220.8	596.0	575.0	746.0	0.965	0.952	1.793
W150×0.7	709.2	1520.4	224.0	217.9	438.9	0.973	1.042	1.763
W180×0.7	760.2	1531.9	236.3	235.2	442.0	0.995	1.050	2.043
W200×0.7	799.3	1182.2	246.5	244.3	436.7	0.991	1.037	2.378

Table 6 PBF processing parameters adopted in this study

Material	Laser type	Laser power (W)	Laser spot size (μm)	Scanning speed (mm/s)	Layer thickness (μm)	Hatch distance (μm)	Scanning rotation (°)	Preheated powder bed (℃)	Preheated powder	Protective gas
316L stainless steel	Yb-fibre	220	100	900	40	100	45	80	No	Argon
CX stainless steel	Yb-fibre	400	100	900	30	100	45	80	No	Argon

Table 7 Measured material properties from vertical (θ=90°) tensile coupon tests

Coupon	E (N/mm^2)	$\sigma_{0.2}$ (N/mm^2)	$\sigma_{1.0}$ (N/mm^2)	σ_u (N/mm^2)	ε_u (%)	ε_f (%)	n	$m_{1.0}$	m_u
316L-1	174100	439	499	551	39.6	60.7	3.4	6.0	7.4
316L-2	162100	420	496	550	45.7	62.0	5.1	7.6	9.4
316L-3	170900	433	502	556	39.7	59.3	3.0	6.6	8.1
316L-4	164400	437	503	555	36.7	59.0	3.0	6.4	7.9
316L-5	172500	443	505	558	35.6	58.5	3.0	5.9	7.2
316L-6	160000	439	502	553	37.4	60.5	3.3	6.2	7.8
Average	167300	435	501	554	39.1	60.0	3.5	6.5	8.0

Table 8 Measured material properties from horizontal (θ=0°) tensile coupon tests

Coupon	E (N/mm^2)	$\sigma_{0.2}$ (N/mm^2)	$\sigma_{1.0}$ (N/mm^2)	σ_u (N/mm^2)	ε_u (%)	ε_f (%)	n	$m_{1.0}$	m_u
CX-1	177200	804	940	1054	6.3	15.9	10.8	4.6	3.6
CX-2	180000	777	924	1046	6.6	20.2	8.2	4.7	3.5
CX-3	180400	779	928	1033	5.9	20.8	8.5	4.7	3.8
CX-4	181300	779	926	1030	6.1	21.2	8.9	4.9	3.9
CX-5	183000	792	934	1052	6.5	21.7	9.8	4.7	3.6
CX-6	183800	775	921	1038	6.2	21.1	8.7	4.5	3.6
Average	181000	784	929	1042	6.3	20.1	9.2	4.7	3.7

Table 9 Measured geometric properties of the test shells and key test results

Specimen	V_{Arch} (mm^3)	V_{laser}^* (mm^3)	L_{cal} (mm)	A_{Arch} (mm^2)	A_{laser}^* (mm^2)	t_{cal} (mm)	ω_{max} (mm)	$\omega_{95\%}$ (mm)	N_u (kN)	δ_u (mm)	$N_u/\sigma_{0.2}A$	$\frac{f_{ult}}{f_{ult,cyl}}$
C200×1.0	93761	95542	152.7	614.0	625.7	1.02	0.19	0.15	366.4	0.57	0.76	-
A200×1.0	152227	154643	199.9	761.5	773.6	1.08	0.51	0.43	601.8	1.31	1.01	1.33
A180×0.7	83380	84782	189.6	439.8	447.2	0.72	0.20	0.13	164.5	0.68	0.86	-
A200×0.7	101073	102993	208.9	483.8	493.0	0.74	0.14	0.08	176.3	0.75	0.84	-
W150×1.0	107071	108452	159.9	669.6	678.2	1.03	0.52	0.37	298.8	1.04	1.03	-
W180×1.0	151174	151425	188.2	803.3	804.6	1.07	0.38	0.29	344.2	1.14	0.99	-
W200×1.0	167332	170572	199.8	837.5	853.7	1.06	0.53	0.30	726.8	1.62	1.11	1.46
W150×0.7	80792	82128	159.7	505.9	514.3	0.76	0.32	0.27	221.0	0.97	1.00	-
W180×0.7	99870	101310	189.5	527.0	534.6	0.75	0.41	0.27	220.5	0.98	0.96	-
W200×0.7	122267	124074	209.7	583.1	591.7	0.73	0.74	0.60	215.3	0.87	0.85	-

* Considered to be less accurate than Archimedes and caliper measurements

Table 10 CDF values and corresponding characteristic imperfection amplitudes measured from shell specimens

$P(\mathbf{\Delta} < \omega_p)$	ω_p (mm)									
	C200×1.0	A200×1.0	A180×0.7	A200×0.7	W150×1.0	W180×1.0	W200×1.0	W150×0.7	W180×0.7	W200×0.7
25%	0.09	0.27	0.04	0.04	0.15	0.15	0.14	0.16	0.16	0.37
50%	0.10	0.31	0.05	0.05	0.19	0.20	0.18	0.19	0.19	0.42
75%	0.11	0.35	0.07	0.06	0.23	0.23	0.23	0.22	0.22	0.47
95%	0.15	0.43	0.13	0.08	0.37	0.29	0.30	0.27	0.27	0.60
99%	0.17	0.48	0.18	0.11	0.45	0.33	0.33	0.30	0.30	0.66
Mean	0.10	0.32	0.06	0.05	0.21	0.19	0.19	0.19	0.19	0.43
Standard deviation	0.02	0.06	0.03	0.02	0.08	0.06	0.07	0.04	0.05	0.09

Table 11 Comparisons of test results with FE results for varying imperfections patterns and amplitudes

Specimen	$N_{u,FE}/N_{u,test}$				$\delta_{u,FE}/\delta_{u,test}$			
	GMNA	GMNIA			GMNA	GMNIA		
		Scan geometry	LBA+$\omega_{95\%}$	LBA+ω_{max}		Scan geometry	LBA+$\omega_{95\%}$	LBA+ω_{max}
C200×1.0	1.19	1.00	0.98	0.93	1.23	0.90	0.89	0.84
A200×1.0	1.09	0.98	1.08	1.08	0.99	0.89	1.13	1.13
A180×0.7	1.03	1.02	1.02	1.00	1.19	1.12	1.20	1.17
A200×0.7	1.05	1.01	1.03	1.00	1.21	1.00	1.10	1.07
W150×1.0	1.04	0.99	1.03	1.03	1.09	0.98	1.09	1.09
W180×1.0	1.02	0.99	1.01	1.01	1.12	1.06	1.13	1.13
W200×1.0	0.95	0.98	0.93	0.92	0.90	0.99	0.91	0.91
W150×0.7	1.00	0.99	1.00	1.00	1.06	1.03	1.05	1.05
W180×0.7	1.04	1.00	1.04	1.04	1.03	1.00	1.04	1.04
W200×0.7	1.07	1.00	1.06	1.06	1.18	1.05	1.19	1.19
Mean	1.05	1.00	1.02	1.01	1.10	1.00	1.07	1.06
COV	0.06	0.01	0.04	0.05	0.10	0.07	0.10	0.10

Table 12 Meridional buckling parameters for medium-length cylinders from EN 1993-1-6

Elastic buckling reduction factor α	Plastic range factor β	Interaction exponent η	Hardening limit χ_h	Squash limit slenderness $\bar{\lambda}_0$	Plastic limit slenderness $\bar{\lambda}_p$
$\frac{0.83}{1+2.2(\Delta\omega_k/t)^{0.88}}$	$1-\frac{0.95}{1+1.2(\Delta\omega_k/t)}$	$\frac{5.4}{1+4.6(\Delta\omega_k/t)}$	1.0	0.2	$\sqrt{\frac{\alpha}{1-\beta}}$

Table 13 Comparisons of experimental and numerical buckling resistances with EN 1993-1-6 resistance predictions for corrugated shells in compression

Evaluation parameter	Test data			FE data		
	No. of results	$N_u/N_{u,EC3}$		No. of results	$N_u/N_{u,EC3}$	
		E_0	E_{sec}		E_0	E_{sec}
Mean	10	1.14	1.44	2764	1.20	1.59
COV		0.11	0.15		0.21	0.39